

# Unexpected Anisotropic Mn-Sb Anti-site Distribution and Van der Waals Epitaxy of $\text{MnSb}_2\text{Te}_4$

Gustavo Chavez Ponce de Leon\*, Ahmad Dibajeh, Gert ten Brink, Majid Ahmadi, Bart Jan Kooi, George Palasantzas\*

MSc. Gustavo Chavez Ponce de Leon

Address: Zernike Institute for Advanced Materials, University of Groningen, 9747 AG Groningen, The Netherlands

Email Address: g.ponce.de.leon@rug.nl

MSc. Ahmad Dibajeh

Address: Zernike Institute for Advanced Materials, University of Groningen, 9747 AG Groningen, The Netherlands

Email Address: a.j.f.dibajeh@rug.nl

Dr. Gert ten Brink

Address: Zernike Institute for Advanced Materials, University of Groningen, 9747 AG Groningen, The Netherlands

Email Address: g.h.ten.brink@rug.nl

Dr. Majid Ahmadi

Addresses: (1) Zernike Institute for Advanced Materials, University of Groningen, 9747 AG Groningen, The Netherlands. (2) CogniGron (Groningen Cognitive Systems and Materials Center), University of Groningen, 9747 AG Groningen, Netherlands.

Email Address: majid.ahmadi@rug.nl

Prof. Dr. Ir. Bart Jan Kooi

Addresses: (1) Zernike Institute for Advanced Materials, University of Groningen, 9747 AG Groningen, The Netherlands. (2) CogniGron (Groningen Cognitive Systems and Materials Center), University of Groningen, 9747 AG Groningen, Netherlands.

Email Address: b.j.kooi@rug.nl

Prof. Dr. George Palasantzas

Addresses: (1) Zernike Institute for Advanced Materials, University of Groningen, 9747 AG Groningen, The Netherlands. (2) CogniGron (Groningen Cognitive Systems and Materials Center), University of Groningen, 9747 AG Groningen, Netherlands.

Email Address: g.palasantzas@rug.nl

Keywords: *Pulsed Laser Deposition [PLD],  $\text{MnSb}_2\text{Te}_4$ , Magnetic Topological Insulator, Van der Waals Epitaxy, Scanning Transmission Electron Microscopy [STEM], Anti-site Defects, Anisotropy*

Mn-Sb site mixing directly impacts both the magnetic and topological properties of  $\text{MnSb}_2\text{Te}_4$ . This study reveals, unlike previously believed, that these anti-sites can be unevenly distributed within the crystal. To that end, a polycrystalline sample was created with a two-step synthesis using  $\text{MnTe}$  and  $\text{Sb}_2\text{Te}_3$  as precursors. DC-SQUID magnetometry was used to confirm its magnetic properties. In addition, the use of High-Resolution Scanning Transmission Electron Microscopy combined with Energy-Dispersive X-ray Spectroscopy allowed us to identify the presence of an inversion-breaking asymmetry in the anti-site distribution. This reduced-symmetry structure bears resemblance to the recently proposed class of Janus materials and thus warrants further exploration due to its potential for combining topology and magnetism with other effects, such as non-linear optics and piezoelectricity. Finally, to further elucidate the interplay between site mixing, doping, topology, and magnetism, a method for growing  $\text{MnSb}_2\text{Te}_4$  thin films over amorphous  $\text{SiO}_x$  using  $\text{Sb}_2\text{Te}_3$  seeds is introduced. The successful Van der Waals epitaxy of  $\text{MnSb}_2\text{Te}_4$  over  $\text{Sb}_2\text{Te}_3$  seeds using Pulsed Laser Deposition is confirmed using Scanning Transmission Electron Microscopy. This represents a crucial step in incorporating these materials into a Si-based architecture, which offers the possibility of controlling the Fermi lever via gating.

# 1 Introduction

In the last decades, chalcogenides-based topological insulators [TIs] (e.g.  $\text{Bi}_2\text{Se}_3$ ,  $\text{Bi}_2\text{Te}_3$ ,  $\text{Sb}_2\text{Te}_3$ , and their alloys) have become a promising class of materials for applications in spintronics, optoelectronics, and quantum computing [1, 2, 3, 4]. While their defining feature of an insulating bulk with conductive surface states is of great interest on its own right [3, 5, 6]; the properties of TIs are significantly bolstered when their surfaces are interfaced with materials exhibiting other physical qualities. For instance, the proximity to superconductors [5, 7], ferromagnets [2, 8, 9] or even other insulators [10], has been linked to exotic phenomena like the elusive Majorana modes [11, 12], the Quantum Anomalous Hall Effect [QAHE] [13, 14], and Weyl states [15, 16].

The close proximity of TIs with these materials, however, is not a trivial enterprise as chalcogenides show an incredibly rich surface chemistry [17, 18, 19]. This, unfortunately, works to the detriment of their qualities, thus hindering the maximum benefits of TIs in current applications. For instance, common electrode like Au or Pt have been reported to react with many TIs creating uncontrolled intermixing layers [18, 19], while the interface with Fe, Co or Ni —standard ferromagnets— has been shown to create a “dead” intermixing layer with neither topological nor magnetic properties [18, 20, 21, 22].

This has shifted the paradigm to search for TIs that naturally combine the presence of topological states with other physical features [2]. For instance, intrinsically magnetic TIs have successfully been created by modulated doping of  $(\text{Bi},\text{Sb})_2\text{Te}_3$  with Cr and V; thereby enabling the observation of the AHE and axion states [2, 23, 24]. Nevertheless, this approach is solely suitable for devices operating at exceedingly low temperatures. Other materials, which inherently incorporate the magnetic atoms into a stoichiometric crystal structure (e.g.  $\text{MnBi}_2\text{Te}_4$  [25],  $\text{MnSb}_2\text{Te}_4$  [26, 27, 28, 29, 30, 31, 32],  $\text{Mn}(\text{Bi},\text{Sb})_2\text{Te}_4$  [33], etc.), have successfully preserved the magnetic order to higher temperatures without sacrificing the signatures of topology.

From this group,  $\text{MnSb}_2\text{Te}_4$  [MST] stands out as one of the TIs with a ferromagnetic order with some of the highest reported Curie temperature [30, 31]. Ideal MST possesses a trigonal  $R\bar{3}m$  (tetradymite) structure, which can be described using a hexagonal unit cell with an A,B,C stacking sequence of close packed planes where covalently boned septuple layers [SL: Te-Sb-Te-Mn-Te-Sb-Te] are separated by a van der Waals [vdW]-like gap [34, 35] (see **Figure 1a**). Similar to its Bi analog ( $\text{MnBi}_2\text{Te}_4$ ), ideal MST is predicted to be a TI with an antiferromagnetic order composed of ferromagnetically ordered Mn planes with an antiferromagnetic interplane coupling where all the magnetic moments align parallel to the crystallographic c-axis [34, 30]. In practice, however, not only has the antiferromagnetic order been observed, but also a ferromagnetic interplane one [27, 33, 29, 28, 30]. This property was quickly linked to the presence of Mn-Sb site mixing [27, 29], which shows significant variation depending on synthesis conditions, thereby explaining the diversity in reported properties.

While the observation of Mn-Sb anti-sites represents an important advancement in understanding MST, not all of its magnetic properties have been fully explained. Indeed, magnetization measurements in the low-temperature region are often accompanied by ‘bumps’ and ‘kinks’ irrespective of the synthesis method [33, 26, 29, 30, 32, 31] strongly suggesting deviations from ideal ferromagnetism. Moreover, even in the paramagnetic phase, MST exhibits deviations from the Curie-Weiss law not present in other similar alloys (e.g.,  $\text{MnBi}_{2-x}\text{Sb}_x\text{Te}_4$ ) [26, 27]. Here, the high-temperature behavior —consistent with an antiferromagnetic order— deviates below  $\sim 50\text{K}-80\text{K}$  to follow a Curie-Weiss law reminiscent of a ferromagnet.

In addition to modifying the magnetic properties, these anti-sites also influence the topological and electrical properties of MST. Indeed, Mn acts as a p-type electrical dopant [36, 37] which, in conjunction with the well-reported tendency of Sb and Te to create heavy p-doped crystals [38, 39, 1, 40], further lowers the Fermi-level away from the bulk bandgap and into the valence band, thus hindering the observation of

---

the exotic properties associated with band topology.

Given that Mn-Sb site mixing governs many of the relevant properties of MST, the need to study the specific spatial distribution of these anti-sites was quickly pointed out [33]. The study by Y. Liu et al. addressed the question using neutron diffraction, where the absence of structured diffuse scattering patterns was indicative of a random distribution of defects, albeit limited by the probe resolution of  $\sim 1\text{nm}$  [29].

In this work, we show that the anti-sites can actually develop an inversion-symmetry-breaking distribution. Our recent Scanning Transmission Electron Microscopy [STEM] results indicate that the Mn-Sb site mixing has a preferential direction, distinguishing between the two Sb planes, where one of the Sb layers presents a higher Mn concentration. The asymmetry is only observed within single septuple layers ( $<1\text{nm}$ ), therefore explaining its absence in neutron scattering experiments. Moreover, the use of Superconductive Quantum Interference Device [SQUID] magnetometry revealed that our sample exhibits hysteresis and remanent magnetization consistent with the ferrimagnetic order.

Finally, in order to address the previously mentioned problem of intrinsic p-doping in as-grown MST, we present a method for growing MST films over amorphous substrates, such as  $\text{SiO}_x$ , which enhances silicon wafer compatibility and thus offers the possibility of controlling the Fermi level via gating. The procedure, commonly referred to as the seeding-layer technique [41, 42, 43], involves a two-step growth where a small layer of amorphous material —the seeds— is initially deposited and subsequently annealed before continuing the high-temperature growth of the desired material. The Van der Waals epitaxy of MST on seeds of  $\text{Sb}_2\text{Te}_3$  using Pulsed Laser Deposition [PLD] is confirmed using atomically resolved STEM.

## 2 Synthesis and Structure

### 2.1 Polycrystalline sample

A polycrystalline ingot of MST was synthesized using a method adapted from Orujiu et al.[44], where the binary compounds MnTe and  $\text{Sb}_2\text{Te}_3$  are used as precursors. The procedure involves an initial high-temperature homogenization phase, followed by quenching, and is concluded with a long annealing period ( $\sim 2$  months) at  $600^\circ\text{C}$  to reach the equilibrium state. These steps are necessary to obtain the  $\text{MnSb}_2\text{Te}_4$  phase since it is not directly accessible through the molten liquid due to a peritectic decomposition ( $\text{MnSb}_2\text{Te}_4 \rightarrow \text{MnTe} + \text{L}$ ) at  $647^\circ\text{C}$  [44]. **Figure 1b** presents a micrograph of the ingot's surface taken with a scanning electron microscope [SEM] operated at  $30\text{kV}$  using a Circular Backscattered [CBS] detector. As can be seen, the sample is composed of a compact network of fairly large crystallites of a couple hundreds of  $\mu\text{m}$  with sharp angular features. The uniform contrast in the CBS image indicates similar composition thought the sample.

The complete incorporation of the precursors is confirmed in **Figure 1d**, where the X-ray diffraction [XRD] spectrum of the sample's powder is compared with the signals expected for  $\text{Sb}_2\text{Te}_3$  [45, 46, 47] (COD ID: 9007590) and MnTe [48, 46, 47] (COD ID: 1539472). The spectrum exactly matches the one reported by Orujiu et al.[44] for MST and does not show the presence of  $\text{Sb}_2\text{Te}_3$  nor MnTe. Moreover, the presence of additional phases like  $\text{MnSb}_4\text{Te}_7$  is also excluded through the small-angle scan. The analysis was repeated for multiple parts of the ingot to confirm its uniformity (**Note S1, Supporting Information**).

A lamella was prepared from the ingot by selecting a suitable oriented grain to display the vdW-like gaps in edge-on orientation. **Figure 1e** presents an inverse pole figure of the sample obtained with electron backscatter diffraction [EBSD], revealing that even after intense grinding, the exposed grains remained large (tens of microns). **Figure 1c** shows the cross-sectional image of the selected grain captured by high-angle annular dark-field [HAADF] STEM. The image shows a nearly perfect arrangement of SL separated

by the vdW-like gap. Furthermore, due to the contrast mechanism of a HAADF detector, where atoms with a lower atomic number appear darker, the atomic arrangement of Mn within a SL can be clearly resolved as shown in the inset of **Figure 1e**. Detailed structural analysis (**Note S2, Supporting Information**) reveals that the contrast variation within a single Mn plane, which was interpreted by Y. Liu et al. [29] as indicative of Mn-Sb site mixing, is absent from our specimen.

Our sample presented few extraneous quintuple layers [QL] or even stacking faults, a common occurrence in layered tellurides [33, 49, 37, 50, 51, 52]. Whenever observed, they would be concentrated near three-dimensional voids (see **Figure 2c**). This observation highlights the role that vacancy ordering plays during crystal formation. Indeed, in analogy with other GeSbTe-based structures, the vacancies likely became mobile during the high-temperature annealing, reconfiguring using the bi-layer defects until reaching the equilibrium MST structure; thus explaining the concentration of these defects solely around the voids [53].

## 2.2 Thin film

MnSb<sub>2</sub>Te<sub>4</sub> films were grown using PLD over thick (~300nm) amorphous SiO<sub>x</sub> aided by Sb<sub>2</sub>Te<sub>3</sub> seeds. The successful Van der Waals epitaxy is both confirmed by the preservation of the Reflection High-Energy Electron Diffraction [RHEED] pattern during growth (**Note S3, Supporting Information**) and by the cross-sectional HAADF-STEM images of **Figure 2a**. Furthermore, the HAADF intensity contrast (**Figure 2b**) confirms that the SLs in the structure are in fact MST with its central Mn planes excluding a possible metastable Sb<sub>4</sub>Te<sub>3</sub> phase [54].

The MST film had an approximate thickness of 23nm and was composed of small (~20nm) randomly in-plane oriented crystallites but with highly-oriented c-axis pointing out-of-plane, a standard signature of the seeding layer technique [43, 55, 56]. These reduced grains created many boundaries and defects, the most abundant of which were bi-layer defects. Frequently, these stacking faults created a complicated pattern in which the SL morphed into QL and even nonuple layers [NL] (see **Figure 2d**). Another common occurrence was the presence of twins and thus twin boundaries (**Figure 2e**); while twinning was observed in both SL and QL, it seemed to occur at a higher frequency between QLs. Moreover, since our samples were exposed to air, the upper surface was exclusively populated with QL, followed by a ~5nm surface oxide.

The need for heteroepitaxy was dictated by the failure to directly use MST as a seeding layer (**Note S3, Supporting Information**). Indeed, the disappearance of RHEED patterns upon annealing strongly suggests that the thin amorphous MST film evaporates before crystallizing, thereby hindering the formation of seeds. In addition (see **Section 3**), the presence of oxygen at the surface stimulated Mn diffusion, further disrupting the crystal formation. Thus, Sb<sub>2</sub>Te<sub>3</sub> offers a proven [54, 57] lattice-matched alternative for the growth of many tellurides over SiO<sub>x</sub>, bearing a strong resemblance to the procedure used by Tamargo et al. [49, 37, 50] for fabricating Sb<sub>2</sub>Te<sub>3</sub>-MnSb<sub>2</sub>Te<sub>4</sub> multilayer.

The final thickness of the film was limited by the appearance of ring-like features in the RHEED pattern (**Note S3, Supporting Information**), indicative of nanocrystal formation whose increased roughness hindered further epitaxy. **Figure 2f** shows a cross-sectional HAADF-STEM image of such a nanocrystal. The structure matches the peritectic decomposition of MST into a liquid Sb<sub>2</sub>Te<sub>3</sub>-rich phase, and MnTe [44], thus confirming that the nanocrystals are not grown on the film but rather transported by the plume after laser ablation. Indeed, the unfortunate presence of particulates on the film surface is a well-reported drawback of PLD [58, 59]; which, nevertheless, could be mitigated by different ablation protocols [59, 60].

### 3 Elemental composition

#### 3.1 Polycrystalline sample

Having confirmed the structure of MST, the elemental distribution was studied with Energy-Dispersive X-ray Spectroscopy [EDS]. The composition of the ingot was confirmed to be uniform and of correct stoichiometry [atomic percentage (error): 14.71% (5.86%) Mn, 28.03% (2.98%) Sb, 57.26% (3.07%) Te]. No additional phases were identified (**Note S4, Supporting Information**).

The atomic resolution elemental map of a single grain is shown in **Figure 3a**. The atomic planes and vdW-like gap are clearly resolved. **Figure 3b** presents their integrated profile. No intermixing is detected on the Te planes. In contrast, in the Mn and Sb planes, and even within the vdW gap, we observe a signal originating from both elements, thereby directly confirming Mn-Sb site mixing and Mn/Sb-interstitials by atomic resolution EDS-STEM. Unexpectedly, the Sb planes show a consistent asymmetry within a single SL: **Figure 3b** shows the Mn signal is higher at the "top" of the SL, while the Sb signal follows the opposite trend. This asymmetry occurs in all SL and is seen across much of the grain (**Note S5, Supporting Information**). Furthermore, unlike observed in the samples by Y. Liu et al. [29], our specimen has fully homogenized atomic planes, thus showing no compositional nor contrast variation perpendicular to the [0001] direction, i.e. in-plane (**Note S2, Supporting Information**).

While asymmetric structures are frequently encountered in crystals synthesized in out-of-equilibrium conditions, like those encountered during molecular beam epitaxy [MBE] [52, 37] or chemical vapor deposition [CVD][61], a kinetic origin of our structure is highly unlikely given our sample's long annealing time ( $\sim 2$  months). Therefore, unlike previously believed [29], MST can actually develop an inversion-symmetry-breaking anti-site distribution at thermodynamic equilibrium.

This surprising observation bears a strong resemblance to the recently proposed class of Janus materials [62, 61, 63] and thus could share both a similar origin and properties. For instance, the asymmetric structure of  $\text{Sb}_2\text{TeSe}_2$  [Janus- $\text{Sb}_2\text{TeSe}_2$ : Te-Sb-Se-Sb-Se, mp-8612], an analogous tetradymite TI [64], is predicted to be more stable than its symmetric counterpart [ $\alpha$ - $\text{Sb}_2\text{TeSe}_2$ : Se-Sb-Te-Sb-Se, mp-571550] [65, 66, 67]. This asymmetry, however, has not been directly confirmed, in contrast with Janus- $\text{Bi}_2\text{TeSe}_2$  [68, 69, 70, 61]. Nonetheless, courtesy of the lower symmetry, Janus structures have been shown to exhibit phenomena not allowed in centrosymmetric structures, such as the Rashba effect[71], polarization-dependent second-harmonic generation[61], and piezoelectricity[72], among others. If similar properties will also be present in MST, which asymmetric structure we have directly demonstrated here, it could offer a platform for combining not just magnetism but also topology with effects like piezoelectricity and non-linear optics, offering a unique platform for topological devices and thus warrants further theoretical and experimental exploration.

#### 3.2 Thin film

The elemental distribution of the MST thin-film is shown in **Figure 3c** with their respective integrated profiles in **Figure 3e**. In contrast with the ingot's single grain, these measurements had a much bigger background contribution due to the small crystallite size; nevertheless, the presence of Mn in the middle of the septuple layers could be directly confirmed with EDS, consistent with the HAADF results (**Figure 2b**), while the asymmetry in the Sb planes was not observed (**Note S5, Supporting Information**). This feature is likely missing due to the out-of-equilibrium conditions involved during film growth.

Since the film was exposed to ambient conditions, a  $\sim 5\text{nm}$  amorphous oxide layer developed at the upper surface. The film was exposed for several days; thus, the layer is presumably self-limiting. A detailed analysis of the different sections of the film (**Figure 3d**) reveals that the top section is Mn-rich and Te-deficient, thus explaining the overabundance of QL at the surface (**Figure 2e**). Indeed, Mn is

---

the element with the strongest oxygen affinity in the compound [73] and thus out-diffuses to form the oxide, arguably making the SL unstable. In this regard, the  $\text{Sb}_2\text{Te}_3$  seeds had an additional effect by preventing the  $\text{SiO}_x$  from reacting with MST, thereby enabling the film growth (**Note S3, Supporting Information**).

Finally, **Figure 3d** presents a comparison of the stoichiometry of the film's core and the ingot, as determined by STEM EDS. There is a strong agreement between the measured percentages, consistent with the well-documented stoichiometric transfer property of PLD [74]. Although the data suggest the film may be Te-deficient, the exact stoichiometry remains within the quantification confidence margins. Nevertheless, a more precise analytical method is recommended to further investigate potential Te loss. Indeed, as presented in other reports [43, 75, 76], chalcogenides' high vapor pressure promotes re-evaporation and material loss during ablation. This may inadvertently favors Mn-Sb intermixing, as Sb must also replace Te in the structure, presumably increasing the p-character of the film. The additional doping, however, might still be compensated by a potential gating enable by the Si-compatible seeding layer.

## 4 Magnetic properties

### 4.1 Polycrystalline sample

To complete the characterization, the magnetic properties of the polycrystalline powder were studied using DC-SQUID magnetometry. **Figure 4a** shows the isothermal magnetization curve at different temperatures. A small but clear hysteresis is observed at 5K which practically vanishes at 25K, in agreement with other reports on (ferri)ferromagnetic MST [27, 29, 28].

The magnetic moment of the sample under -5mT field cooling [FC] is plotted in **Figure 4d**, where a maximum is reached around 20K. The feature is highly sensitive to the cooling conditions and disappears at a moderate field strength (**Note S6, Supporting Information**). While the presence of such a maximum is commonly linked to antiferromagnetic order [77], it has also been reported in (ferri)ferromagnetic samples of  $\text{MnSb}_{1.8}\text{Bi}_{0.2}\text{Te}_4$  [33] and in the in-plane (perpendicular to the crystallographic c-axis) response of  $\text{MnSb}_2\text{Te}_4$  single crystals[29, 32]. Given that in our randomly oriented powder sample the in-plane directions are overrepresented due to the plate-like nature of our specimen (see **Figure 1b**), we suspect that the maximum is in fact caused by the magnetocrystalline anisotropy rather than an antiferromagnetic order.

To further elucidate the magnetic properties, the ratio between the applied field and the magnetic moment is depicted in **Figure 4c**. The quotient is inversely proportional to the susceptibility and thus is expected to follow the Curie-Weiss law above the transition temperature [77]. The linear fit intersects the abscissa at a positive temperature near 25K, consistent with a (ferri)ferromagnetic sample. Nevertheless, when the ratio is measured at higher temperatures (see **Figure 4e**, where the field strength was increased to maintain a high signal-to-noise ratio), the linear trend changes to a smaller slope, thereby shifting the intersection to lower temperatures ( $\sim 4\text{K}$ ).

The paramagnetic anomaly of MST has also been observed by T. Murakami et al.[27], and J.-Q. Yan et al. [26], irrespective of whether the sample exhibits ferri- or antiferromagnetism. The deviation occurs between 50-80K, and was suggested by J.-Q. Yan et al. [26] to be caused by short-range magnetic correlations. Indeed, the higher slope at lower temperature (**Figure 4e**) implies a smaller Curie constant, which signals a "freezing" of effective spins [77]. Noting that all reported MST samples, including ours, have an important amount of Mn-Sb site mixing, we suspect that a mechanism similar to the spin-glass transition of the hematite-ilmenite solid solution may be at play [78]. In this system, the presence of  $\text{Fe}^{3+}$  anti-sites in the  $\text{Ti}^{4+}$  sublattice is believed to produce small regions of antiferromagnetic coupling between  $\text{Fe}^{2+}$ , thereby lowering the effective number of spins. By analogy, the presence of Mn anti-sites in the Sb

planes, together with Mn interstitials within the vdW-like gap (directly observed in **Figure 3a**), could create equivalent antiferromagnetic pockets via a Mn-Te-Mn superexchange [79]. Nevertheless, a detailed microscopic description still needs further development.

The remanent magnetization [RM] after FC is plotted in **Figure 4d**. The RM curves exhibit several unusual features. For instance, when the inverse magnetization is plotted (see **Figure 4f**), the high-temperature anomaly reappears. Moreover, two distinct inflection points are evident in **Figure 4d**. Similar low-temperature traits, significantly deviating from the behavior of an ideal ferromagnet [77], have also been reported in the literature [30, 31]. To our knowledge, these features remain unexplained but may be linked with the small presence of Mn-doped  $\text{Sb}_2\text{Te}_3$  QL, as proposed by Isaeva et al. [31] and Tamargo et al. [37, 50], the latter in the context of  $\text{Sb}_2\text{Te}_3\text{-MnSb}_2\text{Te}_4$  multilayer. Such interpretation aligns well with our observations of QL concentrated near defects, even in seemingly perfect crystals (see **Figure 2c**).

Overall, the observed hysteresis loop and RM provides strong evidence that our sample exhibits ferrimagnetism, consistent with the findings of T. Murakami et al. [27] for polycrystalline MST. Our direct atomic-scale observations reveals extensive Mn site mixing, supporting a structure of ferromagnetic Mn planes antiferromagnetically coupled to Mn anti-sites in Sb planes, as described by Y. Liu et al. [29]. An often overlooked factor in this context is the presence of Mn interstitials, which we have also identified in our long-annealed sample (see **Figure 3b**) and appear to be thermodynamically favored due to increased configurational entropy. Indeed, their presence introduces an additional coupling mechanism that may further enhance ferromagnetic interactions between intra-septuple Mn planes, similar to the behavior observed in other Mn-rich compounds (e.g.  $\text{Mn}_2\text{Sb}_2\text{Te}_5$ ) as reported by Isaeva et al.[80].

## 4.2 Thin film

The DC-SQUID magnetometry results for the MST thin film are plotted in **Figure 4b**. Significant challenges were encountered during the measurements of the thin film sample due to the competing diamagnetic interaction of the  $\text{Si}/\text{SiO}_x$  substrate which severely diminished the total signal. Nevertheless, a clear distinction could still be observed between the out-of-plane (perpendicular to the film) and in-plane response. In neither case, a hysteresis could be observed due to high noise levels.

Courtesy of the seeding layer technique, the out-of-plane direction coincides with the crystallographic c-axis. Contrary to other reports[30, 29], our in-plane response was considerably stronger than the out-of-plane. These observations point to a significant contribution from surface and interface anisotropy [81], likely due to the reduced film thickness and the numerous grain boundaries. Overall, the measurement technique is inadequate to disentangle these contributions; thus, other approaches more suited to the study of magnetization in ultra-thin samples, such as Anomalous Hall measurements[26], should be employed and will be the focus of future research.

## 5 Conclusion

The extraordinary sensitivity of MST to atomic-scale defects establishes atomic structure studies as fundamental for unlocking the mechanisms governing the interplay of topology and magnetism. Such insights not only propel our understanding of MST, but also redefine design principles for next-generation quantum materials. In our work, we have demonstrated that the anti-site distribution of MST can develop, in equilibrium conditions, an anisotropy that clearly distinguishes between the two Sb planes within a SL, while still exhibiting all of its well-reported ferrimagnetic properties [27]. The site mixing is not a universal feature of the compound and depends strongly on synthesis conditions; our research suggests that it develops during long high temperature annealing and is suppressed in out-of equilibrium conditions. The observation of such a structure should warrant further studies and a reevaluation of previous assumptions. For instance, its omission in the expected XRD analyses could misestimate the actual Mn-Sb site mixing

---

of samples. Moreover, it could be an important piece of information for theories aiming to explain MST's magnetic anomalies. In addition, the inversion-symmetry-breaking suggests MST as a prospective member of the emerging class of Janus materials, potentially combining magnetism, topology, and piezoelectricity, among other effects, in a single material.

Lastly, we presented the successful Van der Waals epitaxy of MST over  $\text{Sb}_2\text{Te}_3$ , allowing for its thin film growth over  $\text{SiO}_x$ . Although the seeding-layer approach, has a long history in the growth of chalcogenides-based structures for applications in Phase Change Memory [PCM] and thermoelectrics [43, 54, 57, 55, 56, 82], it has been considerably underexplored in the context of quantum materials, even though its successful use to grow film of materials like the quintessential  $\text{Bi}_2\text{Se}_3$ , with persistent topological properties, has already been demonstrated [83]. The enhanced Si compatibility and the possibility of controlling the effective dopant level via gating, rather than fine-tuning deposition parameters, represent a significant stepping-stone in developing devices based on topology and will undoubtedly play an important role in future research studying the role of carriers in the magnetic and topological properties of MST.

## 6 Experimental Section

### *Solid Synthesis:*

$\text{Sb}_2\text{Te}_3$  was pre-synthesized by mixing 6.490gr of high-purity Sb (99.999% Alfa Aeser) and 10.203gr of Te (99.999% Sigma Aldrich) in an evacuated quartz ampule which was heated up to 700°C (at 5°C/min) in a Nabertherm Box Furnace and left to equilibrate at that temperature for 7hrs followed by a slow cool down to room temperature at a maximum rate of 5°C/min. A small amount of powder was analyzed with XRD (as described below) to confirm the formation of the correct crystal structure (cross-checked with COD ID 9007590 [45]).

The  $\text{MnSb}_2\text{Te}_4$  polycrystalline ingot was synthesized in a two-step procedure using  $\text{MnTe}$  (99.99% Stanford Advanced Materials) and the pre-synthesized  $\text{Sb}_2\text{Te}_3$  as precursors. The method was adapted from the synthesis presented by Oruolu et al. [44]. Firstly, 3.396gr of  $\text{MnTe}$  and 11.647gr of  $\text{Sb}_2\text{Te}_3$  were mixed in a carbon-coated quartz ampule (Sandfire Scientific Ltd.) to avoid any adverse reaction of the Mn with the ampule [44, 84]. The evacuated ampule was heated to 900°C at 1.7°C/min and left for 24hr to homogenize followed by a quenching in icy-water. Secondly, the ampule was annealed at 600°C for 62 days to reach its equilibrium state. Finally, the ampule was cooled down to room temperature at a maximum rate of 2°C/min.

### *Characterization using XRD:*

To obtain the X-ray diffraction [XRD] patterns, both a Bruker D8 Advance and a Bruker D8 Endeavor diffractometers using  $\text{CuK}_\alpha$  radiation at room temperature in the Bragg-Brentano geometry were employed. The powder samples were laid on a Si low background sample holder, and the spectra were recorded between  $2\theta = 15^\circ \div 75^\circ$  ( $5^\circ \div 20^\circ$ ) for 1 sec/measurement (3 sec/meas) at a resolution of 3506 (752) measurements. Many powder samples from different parts of the  $\text{MnSb}_2\text{Te}_4$  ingot were measured to confirm uniformity. In addition, the spectrum of the empty sample holder was also recorded to account for environmental peaks.

### *Characterization using SEM, EDS, and EBSD:*

To expose a flat surface for imaging and elemental mapping, the  $\text{MnSb}_2\text{Te}_4$  ingot was ground using P500, P1000, P2400, and P4000 sandpaper (in that order) with ethanol. In addition, a small piece of the ingot was removed with a blade to be used for lamella preparation. The piece was extensively polished using Ar ion polishing (Gatan PIPS II Model 695); a series of 5kV polishing for 3 hours, 3kV for 2 hours, and 1kV for 1 hour were repeated 4 times to obtain indexable Kikuchi patterns in the Electron Backscattered diffraction [EBSD] signal. The micrographs were taken with a FEI NovaNanoSEM 650 Scanning Electron Microscope [SEM] equipped with a Concentric Backscattered [CBS] and EDAX detector. The elemental composition and uniformity of the target were measured via Energy-Dispersive X-ray Spectroscopy [EDS] by collecting the spectrum from a  $1800 \times 1400 \mu\text{m}^2$  at a resolution of  $512 \times 400$  pixels for about 6 hours with a 10 kV

---

beam with a dwell time of 200  $\mu$ s and 3.84  $\mu$ s amplification time. The spectral deconvolution was performed with the EDAX TEAM software (version 4.6.2004.0297), using the eZAF mode for quantification. Finally, the Kikuchi patterns were collected from a  $44 \times 69 \mu\text{m}^2$  area with a step size of 0.4  $\mu\text{m}$  using a 20 kV beam. The indexing and inverse pole figure were obtained using the OIM Analysis software (version 8.1.0); the latter was performed after a standard grain dilation clean-up procedure.

#### *Growth using PLD:*

The thin films were grown on a  $5 \times 5 \text{ mm}^2$  boron-doped Si wafer piece with 300nm of dry thermal oxide (University wavers ID: 3594). Before every deposition, the substrates were cleaned by sonicating in isopropanol [IPA] for 15 min at 30°C, followed by an IPA flush and drying with a N<sub>2</sub> gun. The samples were glued to the heater in the PLD with a small drop of Ag paint. All depositions were done in a (TSST) Pulsed Laser Deposition [PLD] system using a KrF excimer laser (wavelength of 248nm) with a high-pressure 30 kV Reflection High-Energy Electron Diffraction [RHEED] system for in-situ monitoring. For the Sb<sub>2</sub>Te<sub>3</sub>-MnSb<sub>2</sub>Te<sub>4</sub> films, a laser fluence of 1 J  $\text{cm}^{-2}$  was established before growth started; in addition, a repetition rate of 1 Hz, a target-to-substrate distance of 5.5mm and a processing gas (Ar at 1 sccm) pressure of 0.12mbar were used. The films were grown following the seeding layer procedure [43]; firstly, 150 pulses of a vacuum-sintered powder target of Sb<sub>2</sub>Te<sub>3</sub> (99.99% KTech supplies) were deposited at room temperature to create a thin (3-4nm) layer. Then, the seeds were heated up to 210°C at 5°C/min. After 10 minutes, the growth continued with 3000 pulses of MnSb<sub>2</sub>Te<sub>4</sub> using the synthesized ingot as a target. The sample was then cooled down to room temperature in the same Ar atmosphere. The samples were stored in ambient conditions for 22 days before preparation of a lamella.

#### *Lamella preparation using FIB:*

Electron-transparent samples were prepared in a FEI Helios G5 CX dual-beam SEM-FIB system. A protective C layer, then a Pt layer, was deposited by the electron beam in all cases. This was followed by a thick, ion beam-induced Pt protective layer. A cross-sectional chunk, about  $15 \times 2 \times 5 \mu\text{m}^3$  was extracted and transferred with a W needle to a Cu half-grid. The chunks were then thinned to a final thickness of 80–100 nm using a Ga-beam at 30kV. For all samples, a rigid frame was left to minimize bending and release stress of the electron-transparent window. Finally, several low kV polishing steps (5–2 kV) were applied to remove damage layer and clean the transparent window.

#### *STEM imaging and STEM-EDS analysis:*

The lamellas were mounted on a dedicated double-tilt holder optimized for X-ray collection. Atomic-resolution images were captured with a double-corrected and monochromated (Thermo Fisher Scientific) Themis Z Scanning Transmission Electron Microscope [STEM] operating at 300 kV and equipped with a High-Angle Annular Dark-Field [HAADF] STEM detector, and a 4-segmented (integrated) Differential Phase Contrast [iDPC] annular bright field detector. The beam convergence angle used was 24.0, and 35mrad. A probe current of 20pA was used for imaging. The Energy Dispersive X-ray Spectroscopy [EDS] were measured with a Bruker Dual X EDS system consisting of two large area detectors capturing 1.76 steradian with a probe current of 100pA. The analysis of all STEM images and STEM EDS maps were carried out using the Velox software (version 3.16.1.500). To estimate the stoichiometry of the ingot using STEM EDS, small samples of powder were dispersed in a Cu grid covered with a thin amorphous carbon membrane. Once an electron-transparent particle was found, the elemental map was collected. The process was repeated 5 times to obtain confidence intervals for the stoichiometry. For quantification, all the deconvoluted spectra were analyzed using the Brown-Powell ionization cross-section model after a multi-parabolic background correction.

#### *Characterization using SQUID:*

The magnetic properties of the samples were measured using a Quantum Design Magnetic Property Measurement System [MPMS] XL equipped with a DC-superconductor quantum interference device [SQUID] magnetometer. The powder sample was inserted on a plastic capsule with cotton as support. All samples were suspended from the inserting rod using a plastic straw and Kapton tape. The samples were moved over 6.30cm, collecting 64 points per scan. The average of three scans was used for fitting the magnetic moment to the recorded signal. For magnetization vs field curves, the samples were first cooled down to

the desired temperature, followed by a saturation of the magnetic moment at a field of +5T before starting the measurements.

## Supporting Information

Supporting Information is available from the Wiley Online Library or from the author.

## Acknowledgements

We would like to thank Jacob Baas, Elnur Orujlu, Maxim Mostovoy, and Antonija Grubisic-Cabo for useful discussions; and Javier Chavez Ponce de Leon for his helpful assistance in the preparation of the thumbnail. This research was supported by the Netherlands Organization for Scientific Research (NWO) under Grant No. OTP 19527.

## Conflict of Interest

The author declare no conflict of interest.

## Data Availability Statement

The data that supports the findings of this study are available from the corresponding author upon reasonable request.

## References

- [1] Joseph P Heremans, Robert J Cava, and Nitin Samarth. “Tetradymites as thermoelectrics and topological insulators”. In: *Nature Reviews Materials* 2.10 (2017), pp. 1–21.
- [2] Yoshinori Tokura, Kenji Yasuda, and Atsushi Tsukazaki. “Magnetic topological insulators”. In: *Nature Reviews Physics* 1.2 (2019), pp. 126–143.
- [3] Frank Ortmann, Stephan Roche, and Sergio O Valenzuela. *Topological insulators: Fundamentals and perspectives*. John Wiley & Sons, 2015.
- [4] Qing Lin He et al. “Topological spintronics and magnetoelectronics”. In: *Nature materials* 21.1 (2022), pp. 15–23.
- [5] M Zahid Hasan and Charles L Kane. “Colloquium: topological insulators”. In: *Reviews of modern physics* 82.4 (2010), pp. 3045–3067.
- [6] Xiao-Liang Qi, Taylor L Hughes, and Shou-Cheng Zhang. “Topological field theory of time-reversal invariant insulators”. In: *Physical Review B—Condensed Matter and Materials Physics* 78.19 (2008), p. 195424.
- [7] Hongtao He and Jiannong Wang. “Weak antilocalization effect, quantum oscillation, and superconducting proximity effect in 3D topological insulators”. In: *Topological Insulators: Fundamentals and Perspectives* (2015), pp. 331–355.
- [8] Ke He, Yayu Wang, and Qikun Xue. “Quantum anomalous Hall effect”. In: *Topological Insulators: Fundamentals and Perspectives* (2015), pp. 357–376.
- [9] Anthony Richardella, Abhinav Kandala, and Nitin Samarth. “Topological insulator thin films and heterostructures: Epitaxial growth, transport, and magnetism”. In: *Topological insulators: Fundamentals and perspectives* (2015), pp. 295–329.
- [10] Shuichi Murakami. “Hybridization of topological surface states and emergent states”. In: *Topological Insulators: Fundamentals and Perspectives* (2015), pp. 11–30.
- [11] Liang Fu and Charles L Kane. “Probing neutral Majorana fermion edge modes with charge transport”. In: *Physical review letters* 102.21 (2009), p. 216403.
- [12] Morteza Kayyalha et al. “Absence of evidence for chiral Majorana modes in quantum anomalous Hall-superconductor devices”. In: *Science* 367.6473 (2020), pp. 64–67.
- [13] Rui Yu et al. “Quantized anomalous Hall effect in magnetic topological insulators”. In: *science* 329.5987 (2010), pp. 61–64.
- [14] Cui-Zu Chang et al. “Experimental observation of the quantum anomalous Hall effect in a magnetic topological insulator”. In: *Science* 340.6129 (2013), pp. 167–170.
- [15] AA Burkov and Leon Balents. “Weyl semimetal in a topological insulator multilayer”. In: *Physical review letters* 107.12 (2011), p. 127205.
- [16] N Peter Armitage, Eugene J Mele, and Ashvin Vishwanath. “Weyl and Dirac semimetals in three-dimensional solids”. In: *Reviews of Modern Physics* 90.1 (2018), p. 015001.

[17] Catalin D Spataru and François Léonard. “Fermi-level pinning, charge transfer, and relaxation of spin-momentum locking at metal contacts to topological insulators”. In: *Physical Review B* 90.8 (2014), p. 085115.

[18] Lee A Walsh et al. “Interface chemistry of contact metals and ferromagnets on the topological insulator Bi<sub>2</sub>Se<sub>3</sub>”. In: *The Journal of Physical Chemistry C* 121.42 (2017), pp. 23551–23563.

[19] MC Shaughnessy et al. “Energetics and diffusion of gold in bismuth telluride-based thermoelectric compounds”. In: *Journal of Applied Physics* 115.6 (2014).

[20] RP Gupta et al. “Interface characterization of cobalt contacts on bismuth selenium telluride for thermoelectric devices”. In: *Electrochemical and Solid-State Letters* 12.10 (2009), H395.

[21] Sarmita Majumder et al. “Interfacial reactions at Fe/topological insulator spin contacts”. In: *Journal of Vacuum Science & Technology B* 35.4 (2017).

[22] J Li et al. “Magnetic dead layer at the interface between a Co film and the topological insulator Bi<sub>2</sub>Se<sub>3</sub>”. In: *Physical Review B—Condensed Matter and Materials Physics* 86.5 (2012), p. 054430.

[23] Masataka Mogi et al. “Tailoring tricolor structure of magnetic topological insulator for robust axion insulator”. In: *Science advances* 3.10 (2017), eaao1669.

[24] YL Chen et al. “Massive Dirac fermion on the surface of a magnetically doped topological insulator”. In: *Science* 329.5992 (2010), pp. 659–662.

[25] Mikhail M Otkrov et al. “Prediction and observation of an antiferromagnetic topological insulator”. In: *Nature* 576.7787 (2019), pp. 416–422.

[26] J-Q Yan et al. “Evolution of structural, magnetic, and transport properties in MnBi<sub>2-x</sub>Sb<sub>x</sub>Te<sub>4</sub>”. In: *Physical Review B* 100.10 (2019), p. 104409.

[27] Taito Murakami et al. “Realization of interlayer ferromagnetic interaction in MnS<sub>2</sub>T<sub>4</sub> toward the magnetic Weyl semimetal state”. In: *Physical Review B* 100.19 (2019), p. 195103.

[28] Wenbo Ge et al. “Direct evidence of ferromagnetism in MnSb<sub>2</sub>Te<sub>4</sub>”. In: *Physical Review B* 103.13 (2021), p. 134403.

[29] Yaohua Liu et al. “Site mixing for engineering magnetic topological insulators”. In: *Physical Review X* 11.2 (2021), p. 021033.

[30] Stefan Wimmer et al. “Mn-Rich MnSb<sub>2</sub>Te<sub>4</sub>: A topological insulator with magnetic gap closing at high curie temperatures of 45–50 K”. In: *Advanced Materials* 33.42 (2021), p. 2102935.

[31] Laura C Folkers et al. “Occupancy disorder in the magnetic topological insulator candidate Mn<sub>1-x</sub>Sb<sub>2+x</sub>Te<sub>4</sub>”. In: *Zeitschrift für Kristallographie-Crystalline Materials* 237.4-5 (2022), pp. 101–108.

[32] Ming Xi et al. “Relationship between antisite defects, magnetism, and band topology in MnSb<sub>2</sub>Te<sub>4</sub> crystals with TC ≈ 40 K”. In: *The Journal of Physical Chemistry Letters* 13.47 (2022), pp. 10897–10904.

[33] Yangyang Chen et al. “Ferromagnetism in van der Waals compound MnS<sub>2</sub>Te<sub>4</sub>”. In: *Physical Review Materials* 4.6 (2020), p. 064411.

[34] Sergey V Eremeev, MM Otkrov, and Eugene V Chulkov. “Competing rhombohedral and monoclinic crystal structures in MnPn<sub>2</sub>Ch<sub>4</sub> compounds: An ab-initio study”. In: *Journal of Alloys and Compounds* 709 (2017), pp. 172–178.

[35] Bart J Kooi and Matthias Wuttig. “Chalcogenides by design: functionality through metavalent bonding and confinement”. In: *Advanced materials* 32.21 (2020), p. 1908302.

[36] Haixu Qin et al. “Achieving a high average zT value in Sb<sub>2</sub>Te<sub>3</sub>-based segmented thermoelectric materials”. In: *ACS Applied Materials & Interfaces* 12.1 (2019), pp. 945–952.

[37] Ido Levy et al. “High Curie temperature ferromagnetic structures of (Sb<sub>2</sub>Te<sub>3</sub>)<sub>1-x</sub>(MnSb<sub>2</sub>Te<sub>4</sub>)<sub>x</sub> with x = 0.7–0.8”. In: *Scientific Reports* 13.1 (2023), p. 7381.

[38] David Hsieh et al. “Observation of Time-Reversal-Protected Single-Dirac-Cone Topological-Insulator States in Bi<sub>2</sub>Te<sub>3</sub> and Sb<sub>2</sub>Te<sub>3</sub>”. In: *Physical review letters* 103.14 (2009), p. 146401.

[39] Guang Wang et al. “Atomically smooth ultrathin films of topological insulator Sb<sub>2</sub>Te<sub>3</sub>”. In: *Nano Research* 3.12 (2010), pp. 874–880.

[40] Hwansoo Suh. “Probing Topological Insulator Surface States by Scanning Tunneling Microscope”. In: *Topological Insulators: Fundamentals and Perspectives* (2015), pp. 217–244.

[41] Yuta Saito et al. “Self-organized van der Waals epitaxy of layered chalcogenide structures”. In: *physica status solidi (b)* 252.10 (2015), pp. 2151–2158.

[42] LJ Collins-McIntyre et al. “Growth of Bi Se and Bi Te on amorphous fused silica by MBE”. In: *physica status solidi (b)* 252.6 (2015), pp. 1334–1338.

[43] {Paul Alexander} Vermeulen. "Growth and nanostructure of tellurides for optoelectronic, thermoelectric and phase-change applications". English. PhD thesis. University of Groningen, 2019. ISBN: 978-94-034-1422-5.

[44] EN Oruju et al. "Phase equilibria of the MnTe-Sb<sub>2</sub>Te<sub>3</sub> system and synthesis of novel ternary layered compound—MnSb<sub>4</sub>Te<sub>7</sub>". In: *Physics and Chemistry of Solid State* 22.1 (2021), pp. 39–44.

[45] THOMAS L Anderson and H BRIGITTE Krause. "Refinement of the Sb<sub>2</sub>Te<sub>3</sub> and Sb<sub>2</sub>Te<sub>2</sub>Se structures and their relationship to nonstoichiometric Sb<sub>2</sub>Te<sub>3</sub>-ySe compounds". In: *Structural Science* 30.5 (1974), pp. 1307–1310.

[46] R. T. Downs and M. Hall-Wallace. "The American Mineralogist Crystal Structure Database". In: *American Mineralogist* 88 (2003), pp. 247–250.

[47] Saulius Gražulis et al. "Crystallography Open Database – an open-access collection of crystal structures". In: *Journal of Applied Crystallography* 42.4 (Aug. 2009), pp. 726–729. DOI: 10.1107/S0021889809016690. URL: <https://doi.org/10.1107/S0021889809016690>.

[48] OL Kruger and JB Moser. "Lattice constants and melting points of actinide-group IVA-VIA compounds with NaCl-type structures". In: *Journal of Physics and Chemistry of Solids* 28.11 (1967), pp. 2321–2325.

[49] Ido Levy et al. "Compositional control and optimization of molecular beam epitaxial growth of (Sb<sub>2</sub>Te<sub>3</sub>) 1-x (MnSb<sub>2</sub>Te<sub>4</sub>) x magnetic topological insulators". In: *Crystal Growth & Design* 22.5 (2022), pp. 3007–3015.

[50] Candice R Forrester et al. "Structural and magnetic properties of molecular beam epitaxy (MnSb<sub>2</sub>Te<sub>4</sub>) x (Sb<sub>2</sub>Te<sub>3</sub>) 1-x topological materials with exceedingly high Curie temperature". In: *APL Materials* 12.7 (2024).

[51] Jamo Momand et al. "Interface formation of two-and three-dimensionally bonded materials in the case of GeTe–Sb 2 Te 3 superlattices". In: *Nanoscale* 7.45 (2015), pp. 19136–19143.

[52] Jamo Momand et al. "Atomic stacking and van-der-Waals bonding in GeTe–Sb<sub>2</sub>Te<sub>3</sub> superlattices". In: *Journal of Materials Research* 31.20 (2016), pp. 3115–3124.

[53] Jamo Momand et al. "Dynamic reconfiguration of van der Waals gaps within GeTe–Sb 2 Te 3 based superlattices". In: *Nanoscale* 9.25 (2017), pp. 8774–8780.

[54] Daniel T Yimam, Majid Ahmadi, and Bart J Kooi. "Van der Waals epitaxy of pulsed laser deposited antimony thin films on lattice-matched and amorphous substrates". In: *Materials Today Nano* 23 (2023), p. 100365.

[55] Daniel Yimam. "Phase-change thin films growth and functionality: towards phase-change memory and reconfigurable nanophotonics". English. PhD thesis. University of Groningen, 2023. DOI: 10.33612/diss.622460932.

[56] Jama Momand. "Structure and reconfiguration of epitaxial GeTe/Sb<sub>2</sub>Te<sub>3</sub> superlattices". English. PhD thesis. University of Groningen, 2017. ISBN: 978-94-034-0189-8.

[57] Paul A Vermeulen et al. "Strain engineering of van der Waals heterostructures". In: *Nanoscale* 10.3 (2018), pp. 1474–1480.

[58] Stephen J Barrington et al. "The effect of particulate density on performance of Nd: Gd<sub>3</sub>Ga<sub>5</sub>O<sub>12</sub> waveguide lasers grown by pulsed laser deposition". In: *Optics communications* 185.1-3 (2000), pp. 145–152.

[59] Daniel T Yimam et al. "Pulsed laser deposited stoichiometric GaSb films for optoelectronic and phase change memory applications". In: *Materials Science in Semiconductor Processing* 133 (2021), p. 105965.

[60] Peter K Schenck et al. "Particulate reduction in the pulsed laser deposition of barium titanate thin films". In: *Applied surface science* 127 (1998), pp. 655–661.

[61] Xiaobin Zou et al. "Unusual Janus Bi<sub>2</sub>TeSe<sub>2</sub> Topological Insulators Displaying Second-Harmonic Generation, Linear-in-Temperature Resistivity, and Weak Antilocalization". In: *Journal of the American Chemical Society* 146.26 (2024), pp. 17784–17792.

[62] Xinfeng Chen et al. "Screening vertically polarized 2D layered materials with giant negative longitudinal piezoelectricity by comprehensive calculations and experimental characterizations". In: *Advanced Functional Materials* 34.52 (2024), p. 2410675.

[63] Jiawei Jiang et al. "Topological spin textures in a two-dimensional MnBi<sub>2</sub> (Se, Te) 4 Janus material". In: *Applied Physics Letters* 119.7 (2021).

[64] Tien-Tien Yeh et al. "Femtosecond time-evolution of mid-infrared spectral line shapes of Dirac fermions in topological insulators". In: *Scientific reports* 10.1 (2020), p. 9803.

[65] Anubhav Jain et al. "Commentary: The Materials Project: A materials genome approach to accelerating materials innovation". In: *APL materials* 1.1 (2013).

[66] Anubhav Jain et al. "Formation enthalpies by mixing GGA and GGA+U calculations". In: *Physical Review B—Condensed Matter and Materials Physics* 84.4 (2011), p. 045115.

[67] Ying Chen et al. "New Sb<sub>2</sub>Te<sub>3</sub>-x Se x monolayers with high electron mobilities and wide absorption range". In: *ACS Applied Materials & Interfaces* 11.40 (2019), pp. 37216–37228.

[68] Michael Küpers et al. "Preferred selenium incorporation and unexpected interlayer bonding in the layered structure of Sb<sub>2</sub>Te<sub>3-x</sub>Se<sub>x</sub>". In: *Zeitschrift für Naturforschung B* 75.1-2 (2020), pp. 41–50.

[69] Iwao Teramoto and Shigetoshi Takayanagi. "Relations between the electronic properties and the chemical bonding of SbxBi2-xTe3-ySe<sub>y</sub> system". In: *Journal of Physics and Chemistry of Solids* 19.1-2 (1961), pp. 124–129.

[70] Carolien Callaert. "Characterization of defects, modulations and surface layers in topological insulators and structurally related compounds". English. PhD thesis. Universiteit Antwerpen, 2020.

[71] Lei Zhang, Yuantong Gu, and Aijun Du. "Two-dimensional Janus antimony selenium telluride with large Rashba spin splitting and high electron mobility". In: *ACS omega* 6.47 (2021), pp. 31919–31925.

[72] Jian Qiu et al. "Piezoelectricity of Janus Sb<sub>2</sub>Se<sub>2</sub>Te monolayers: A first-principles study". In: *Journal of Applied Physics* 129.12 (2021).

[73] Klaus A Moltved and Kasper P Kepp. "The chemical bond between transition metals and oxygen: electronegativity, d-orbital effects, and oxophilicity as descriptors of metal–oxygen interactions". In: *The Journal of Physical Chemistry C* 123.30 (2019), pp. 18432–18444.

[74] Guus Rijnders and Dave HA Blank. "In situ diagnostics by high-pressure RHEED during PLD". In: *Pulsed laser deposition of thin films* (2006), pp. 85–97.

[75] P Orgiani et al. "Structural and electronic properties of Bi<sub>2</sub>Se<sub>3</sub> topological insulator thin films grown by pulsed laser deposition". In: *Applied Physics Letters* 110.17 (2017).

[76] H Noro, K Sato, and H Kagechika. "The thermoelectric properties and crystallography of Bi-Sb-Te-Se thin films grown by ion beam sputtering". In: *Journal of Applied Physics* 73.3 (1993), pp. 1252–1260.

[77] Stephen Blundell. *Magnetism in condensed matter*. OUP Oxford, 2001.

[78] NE Brown et al. "Hematite-ilmenite (Fe<sub>2</sub>O<sub>3</sub>-FeTiO<sub>3</sub>) solid solutions: Determinations of Fe-Ti order from magnetic properties". In: *American Mineralogist* 78.9-10 (1993), pp. 941–951.

[79] Jian-Min Zhang et al. "Stability, electronic, and magnetic properties of the magnetically doped topological insulators Bi<sub>2</sub>Se<sub>3</sub>, Bi<sub>2</sub>Te<sub>3</sub>, and Sb<sub>2</sub>Te<sub>3</sub>". In: *Phys. Rev. B* 88 (23 Dec. 2013), p. 235131. DOI: 10.1103/PhysRevB.88.235131. URL: <https://link.aps.org/doi/10.1103/PhysRevB.88.235131>.

[80] Ekaterina Kochetkova et al. "Mn Interstitials in Layered Mn<sub>1+x</sub>Sb<sub>2-2/3</sub>xTe<sub>4</sub>: Structural Modification and Curie Temperature Boost". In: *Chemistry of Materials* 37.4 (2025), pp. 1446–1456.

[81] Gayanath W Fernando. "Magnetic anisotropy in transition metal systems". In: *Handbook of Metal Physics*. Vol. 4. Elsevier, 2008, pp. 89–110.

[82] Chao Nie et al. "Role of seed layer in growing atomically flat TiTe<sub>2</sub>/Sb<sub>2</sub>Te<sub>3</sub> heterostructure thin films at the wafer scale". In: *Advanced Materials Interfaces* (2025), e00455.

[83] Namrata Bansal et al. "Robust topological surface states of Bi<sub>2</sub>Se<sub>3</sub> thin films on amorphous SiO<sub>2</sub>/Si substrate and a large ambipolar gating effect". In: *Applied Physics Letters* 104.24 (2014).

[84] Vincent Canaguier and Merete Tangstad. "Kinetics of slag reduction in silicomanganese production". In: *Metallurgical and Materials Transactions B* 51.3 (2020), pp. 953–962.

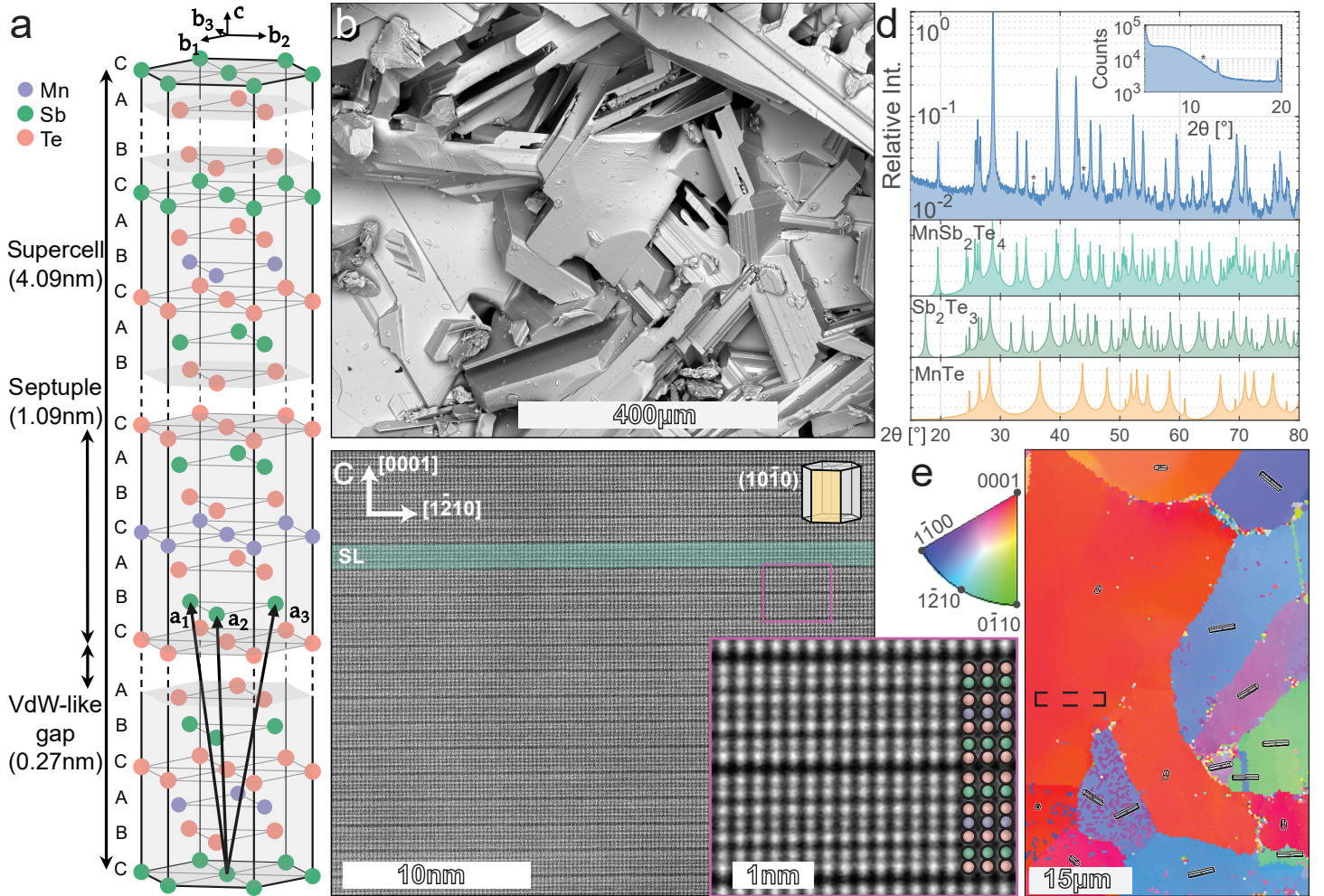


Figure 1: Characterization of polycrystalline MnSb<sub>2</sub>Te<sub>4</sub> sample. a) Schematic representation of the ideal crystal structure. The a-vectors indicate the primitive rhombohedral cell, while the b-vectors represent the hexagonal supercell. b) CBS SEM micrograph of the ingot as-synthesized, the crystallites have a considerable size of a couple hundreds of microns exhibiting sharp angular features. No compositional contrast is observed indicative of the ingot's uniformity. c) HAADF STEM images of a single grain. The crystal consists of perfectly arranged SL separated by a Van der Waals-like gap. The inset shows a zoom in version of the SL captured using drift corrected frame integration [DCFI] and post-processed with a radial Wiener filter. The difference in contrast due to atomic number clearly highlights the location of Mn in the structure. d) XRD of the polycrystalline sample compared with the simulated pattern of MnSb<sub>2</sub>Te<sub>4</sub> (as reported by [44]) and its precursors (Sb<sub>2</sub>Te<sub>3</sub> [45] and MnTe [48]). The asterisk indicate background peaks. e) Inverse pole figure of the gridded ingot obtained using EBSD. The selected area indicates the approximate location where the lamella was taken.

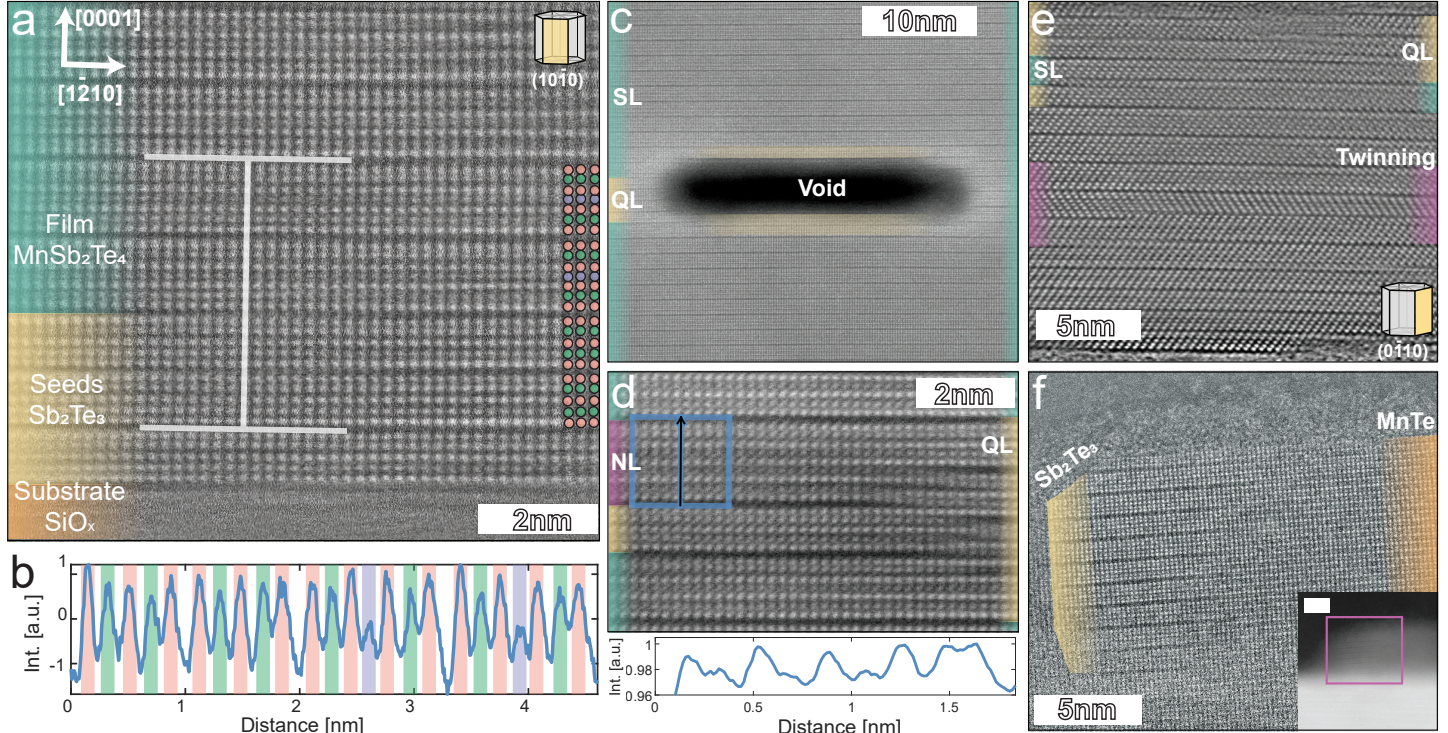


Figure 2: Structure and defects of  $\text{MnSb}_2\text{Te}_4$ . a) HAADF STEM images of the thin film. SL of  $\text{MnSb}_2\text{Te}_4$  are epitaxially grown over three QLs of  $\text{Sb}_2\text{Te}_3$  seeds over amorphous  $\text{SiO}_x$ . b) Intensity profile of the area marked in (a), the contrast in the HAADF image is generated by difference in atomic number enabling the identification of Mn in the structure. The Sb peaks show slight contrast variation from the Te suggesting Mn-Sb site mixing. c) HAADF STEM image of a single  $\text{MnSb}_2\text{Te}_4$  grain. The only defects found in the grain were 3D voids where occasional QL (in yellow) could be found. d) HAADF STEM image with a Radial Wiener filter of the  $\text{MnSb}_2\text{Te}_4$  thin film. Abundant bilayer defects are present which mediate the position of QL and SL in the film. Occasionally they even combine to form nonuple layers [NL]. Its corresponding intensity profile is plotted below. e) iDPC STEM image of the MST film showing a twin boundary. Due to oxidation, only QL can be bound at the upper surface of the film. f) HAADF STEM image of a particulate in the surface of the film transported during pulsed laser deposition. The particulate shows the peritectic decomposition of  $\text{MnSb}_2\text{Te}_4$  into MnTe and  $\text{Sb}_2\text{Te}_3$ .

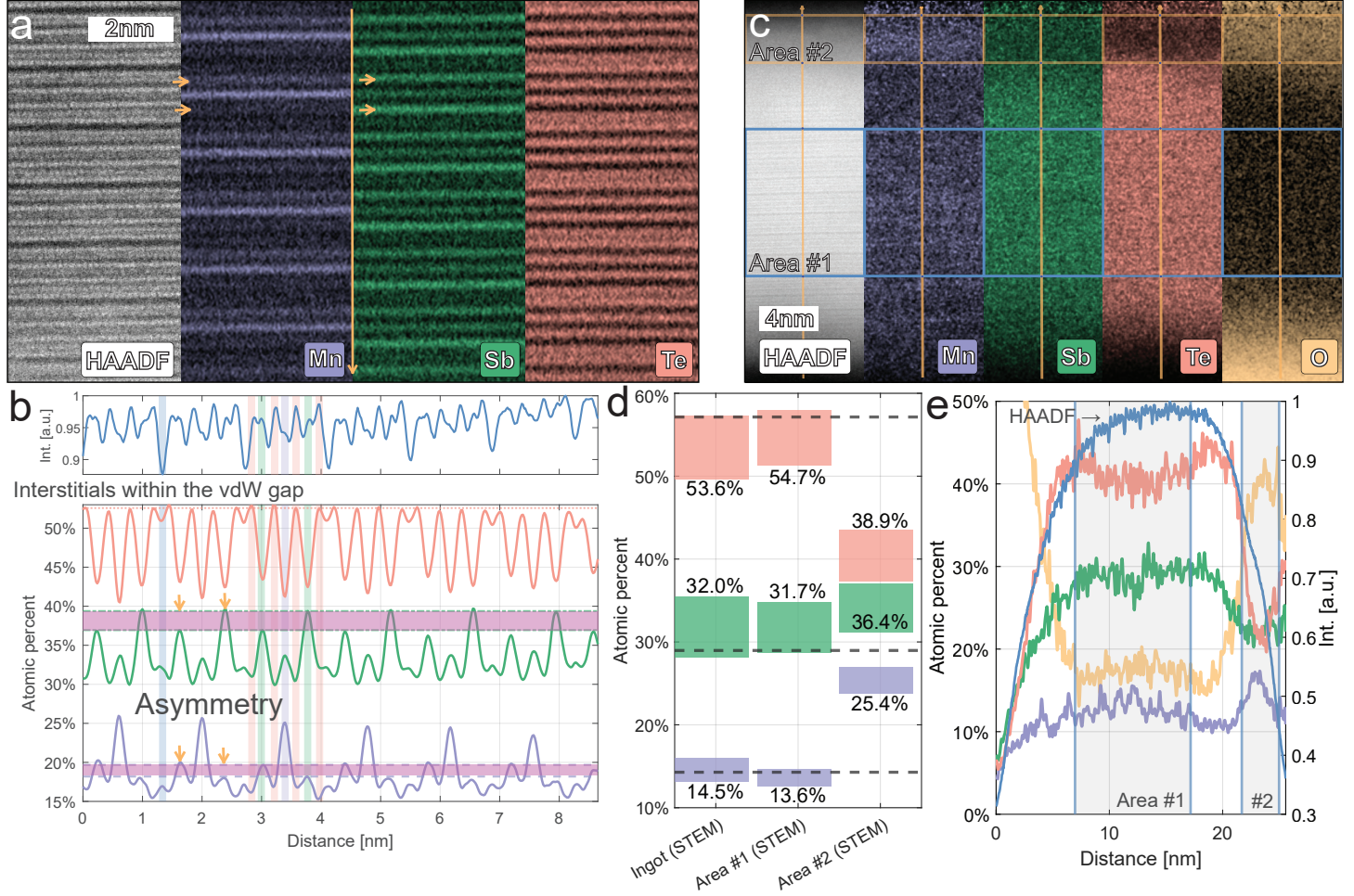
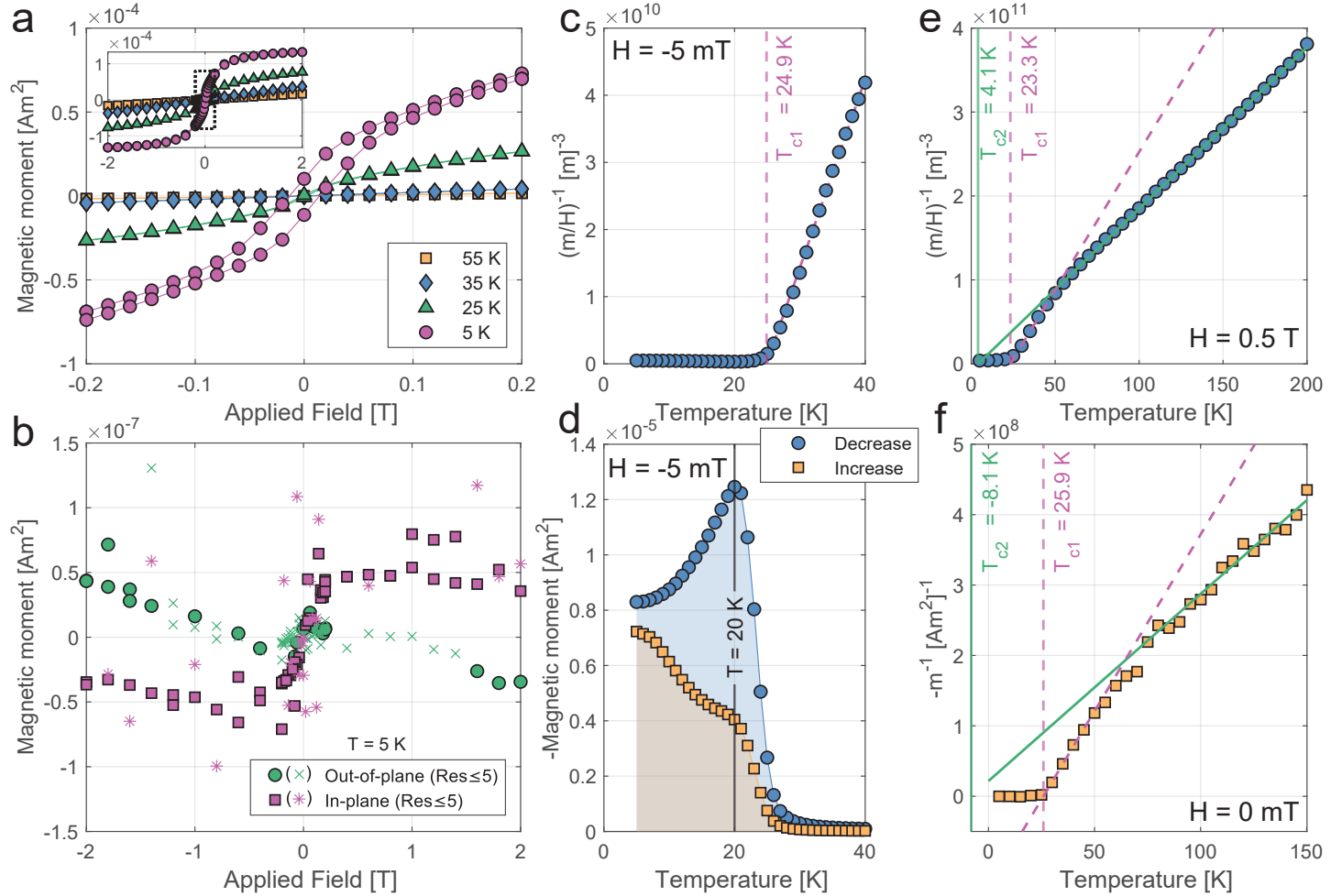


Figure 3: Stochiometry and atomic distribution in  $\text{MnSb}_2\text{Te}_4$ . a) Atomically resolved elemental map of a single  $\text{MnSb}_2\text{Te}_4$  grain measured with EDS in STEM mode (integration over 5581 frames). The Mn-Sb anti-sites are asymmetrically distributed. b) Intensity profiles corresponding to Fig. (a) with integration width of 16 nm. A significant Mn signal can be found in the Sb planes and even within the Van der Waals gap as interstitials. The orange arrows indicate the asymmetry in the Sb planes with one plane showing more Mn signal and correspondingly less Sb. The asymmetry occurs within a septuple layer and it is consistent in all septuple layers and multiple parts of the grain. No asymmetry in the Te planes is detected. c) Elemental distribution within the thin film. In the presence of oxygen, Mn diffuses from the center of the film (area #1) to the surface (area #2) creating a Mn-rich amorphous oxide. d) Stoichiometry of the ingot (as determined by EDS in STEM mode), the bulk of the film, and the amorphous oxide (areas #1 and #2 in Fig. (c) respectively). e) Line profile of Fig. (c). The HAADF signal is plotted in blue and corresponds to the right-side axis. The increase of Mn and O near the surfaces is clearly visible.



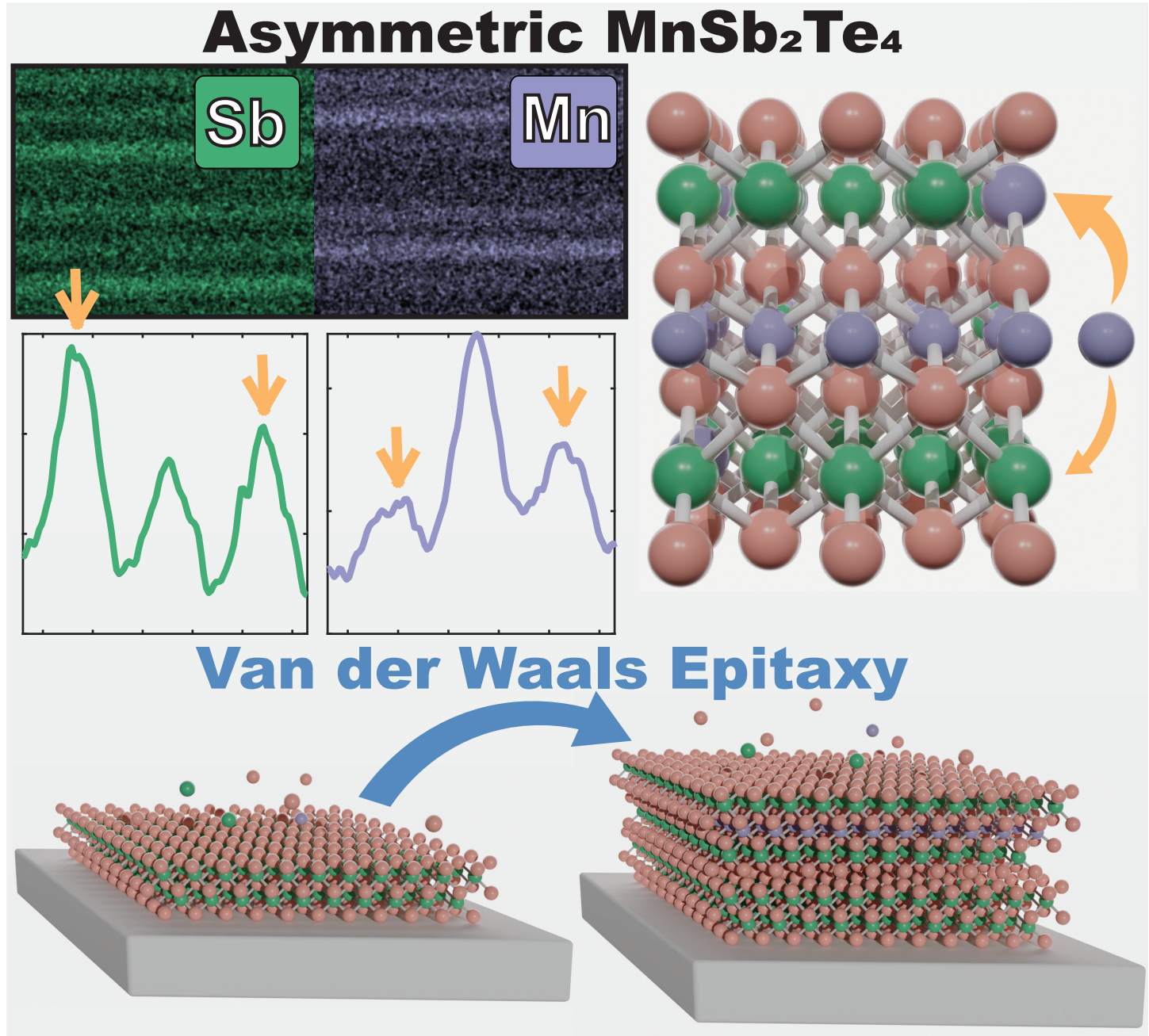


Figure 5: Table of content/Thumbnail figure

# Supporting Information of: Unexpected Anisotropic Mn-Sb Anti-site Distribution and Van der Waals Epitaxy of $\text{MnSb}_2\text{Te}_4$

by Gustavo Chavez Ponce de Leon ([g.ponce.de.leon@rug.nl](mailto:g.ponce.de.leon@rug.nl)), Ahmad Dibajeh ([a.j.f.dibajeh@rug.nl](mailto:a.j.f.dibajeh@rug.nl)), Gert ten Brink ([g.h.ten.brink@rug.nl](mailto:g.h.ten.brink@rug.nl)), Majid Ahmadi ([majid.ahmadi@rug.nl](mailto:majid.ahmadi@rug.nl)), Bart Jan Kooi ([b.j.kooi@rug.nl](mailto:b.j.kooi@rug.nl)), George Palasantzas ([g.palasantzas@rug.nl](mailto:g.palasantzas@rug.nl)).

## Content

- S1: XRD of powder samples from different parts of the ingot
- S2: Detailed structural analysis of STEM pictures
- S3: RHEED data of additional thin film depositions
- S4: EDS of solid ingot
- S5: Additional atomically-resolved EDS maps (ingot and thin film)
- S6: Additional magnetization plots

**S1: XRD of powder samples from different parts of the ingot**

To confirm the uniformity of the synthesized ingot, powder samples were collected from different parts hereby named: top, middle, bottom. Their respective XRD spectrum are plotted in **Figure S1**. The position and intensity of all peaks are consistent with each other.

The morphology of the powder was “flake-like” (see **Figure 1b** of the main text); thus, the relative peak amplitude measured experimentally is expected to differ from the theoretical values, which assume an isotropic powder.

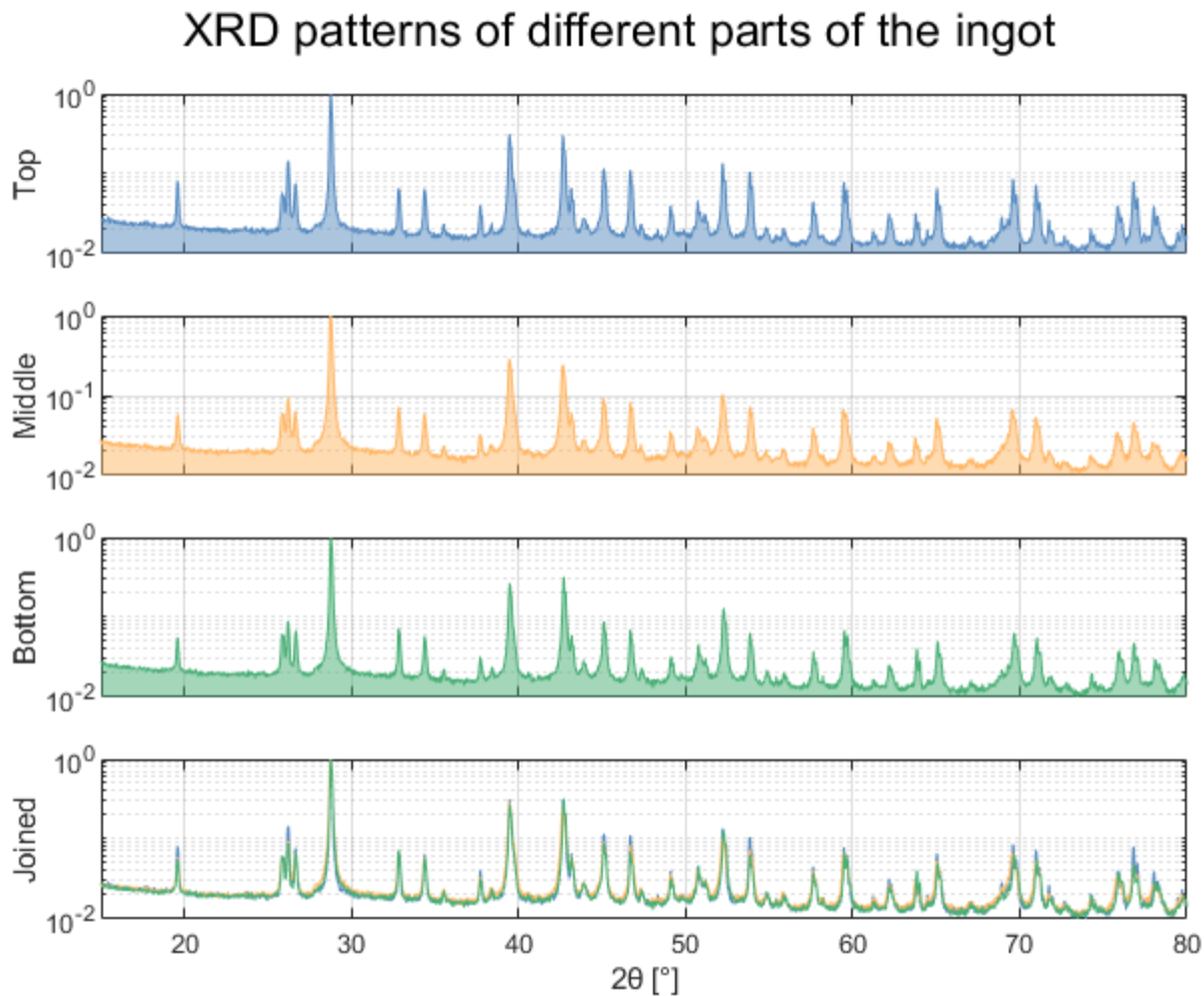


*Figure S1: Additional XRD spectra of the synthesized ingot. The uniformity of the target is confirmed by the overlapping graphs.*

## S2: Detailed structural analysis of STEM pictures

In this section, we present a more detailed analysis of the HAADF-STEM images of the MST single grain.

To begin, we study the in-plane intensity variations of each atomic plane. As can be seen from **Figure S2.1**, regardless of the atomic plane, the contrast remains fairly constant. This observation suggests that, while our sample exhibits an asymmetric distribution of antisites along the crystallographic c-axis (as explained in the main text), they are uniformly distributed in-plane. This differs from the observation of Y. Liu et al [Yaohua Liu et al. "Site mixing for engineering magnetic topological insulators". In: Physical Review X 11.2 (2021), p. 021033.], which shows in-plane intensity variations in the Mn planes indicative not only of Mn-Sb site-mixing but also of their non-uniformity within each atomic plane.

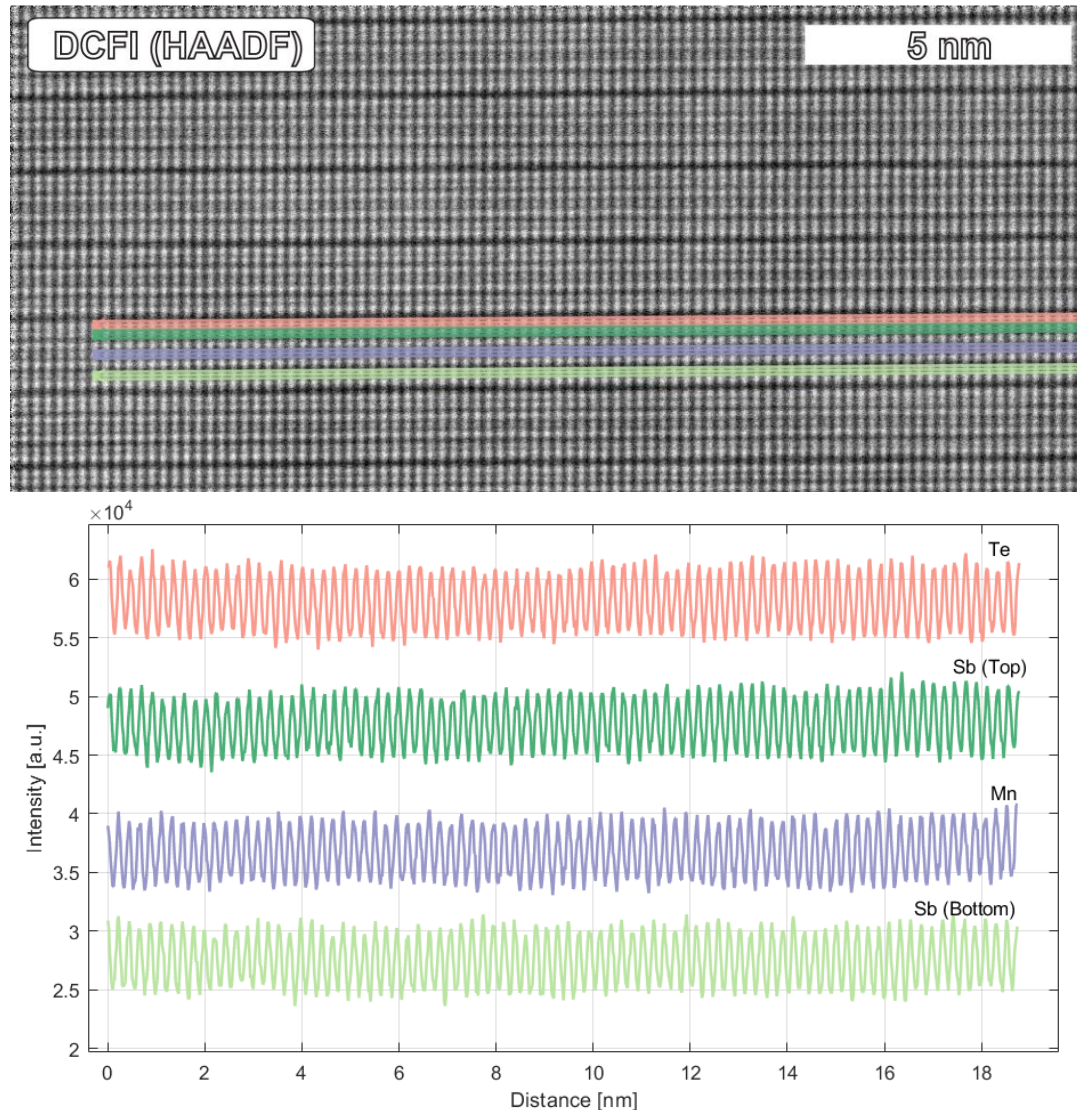


*Figure S2.1: In-plane intensity variation of a single MST grain. All the atomic layers show a fairly uniform contrast indicative of a homogeneously in-plane sample. Only vertical offsets were applied to the intensities.*

Next, the STEM-HAADF images were analyzed using the Atomap Python library [<https://atomap.org/>]. In the analysis, 2-D Gaussian functions are fitted to every atomic column, which allows for the quantification of interplanar distance perpendicular to the vdW gap; the results are illustrated in **Figure S2.2**.

Unlike the compositional asymmetry reported in section 3.1 of the main text, no structural asymmetry could be systematically determined between the different planes composing a single septuplet layer. Thus, it appears that the difference in site mixing between the Sb planes is small enough to not introduce significant strain.

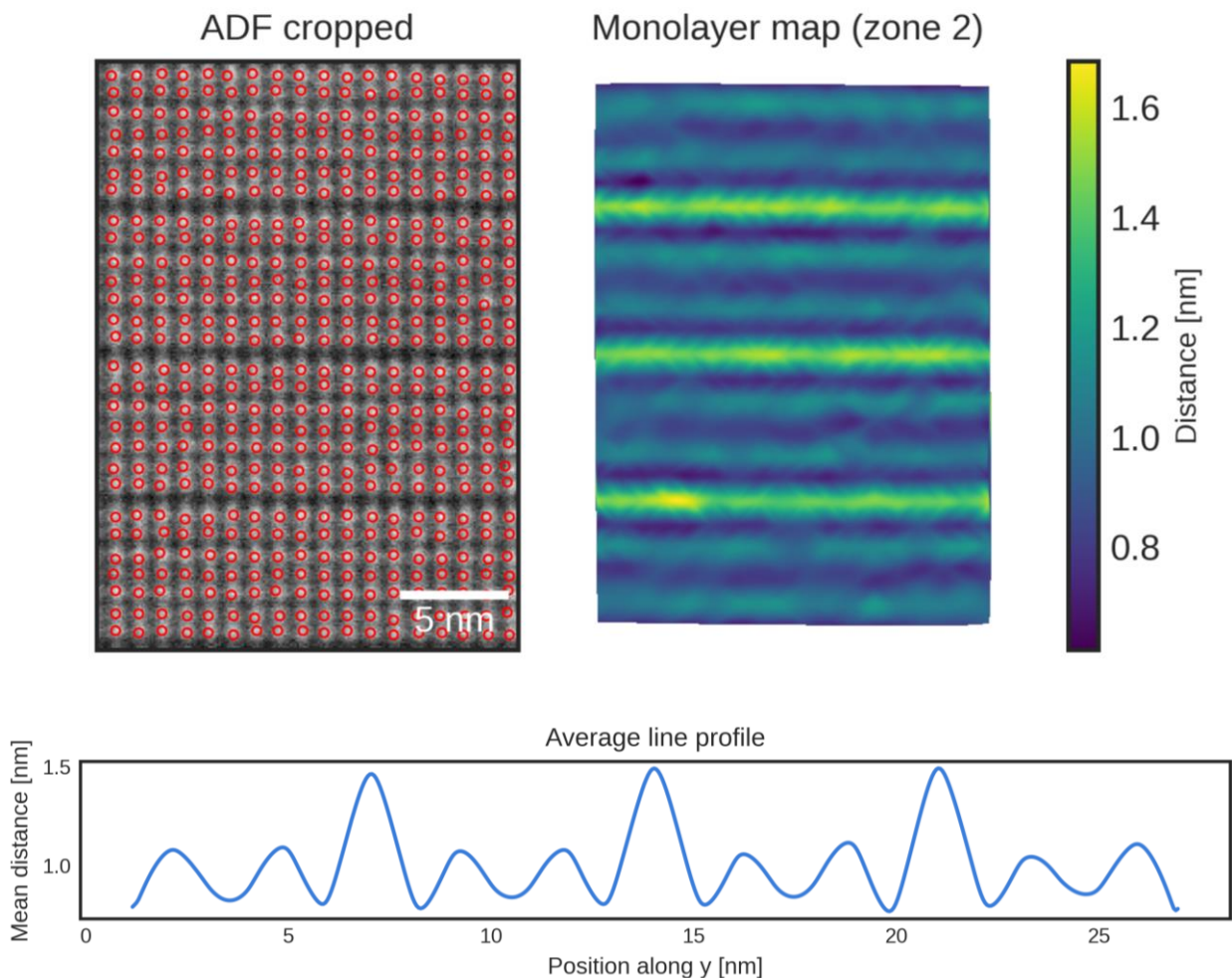


*Figure S2.2: Analysis of STEM-HAADF images using the Atomap Python library. The atomic positions are found by fitting 2-D gaussians. The large separation in interplanar distance corresponds to the vdW-like gap. No systematic structural asymmetry could be determined within a single septuplet layer.*

### S3: RHEED data of additional thin film depositions

In this section, we present the results of in-situ RHEED measurements during film growth.

#### S3.1: Seeding layer of MST.

Our attempts to use MST as the seeds are shown in **Figures S3.1.1 and S3.1.2**. The experiments consisted of depositing MST at room temperature (30°C) in an Ar atmosphere with a process pressure of 1.2E-1mbar, using 1J/cm<sup>2</sup> fluence. The RHEED pattern displayed at Time: 0.00s (see **Figure S3.1.1**) shows no particular features as expected from an amorphous SiO<sub>x</sub> substrate. As the film grows, the pattern starts to display ring-like features indicative of the presence of nanocrystals in the substrate. The situation is similar to Sb<sub>2</sub>Te<sub>3</sub> seeds (as will be shown in **Section S3.2**) and Bi<sub>2</sub>Te<sub>3</sub> [Vermeulen. "Growth and nanostructure of tellurides for optoelectronic, thermoelectric and phase-change applications". English. PhD thesis. University of Groningen, 2019. isbn: 978-94-034-1422-5. Daniel Yimam. "Phase-change thin films growth and functionality: towards phase-change memory and reconfigurable nanophotonics". English. PhD thesis. University of Groningen, 2023. doi: 10.33612/diss.622460932].

The final thickness of the film was determined to be around 4nm, which corresponds to a growth rate of 1nm for 100 pulses. This rate was determined by previous experiments using an Atomic Force Microscope [AFM], where the film was gently scratched with plastic tweezers and the thickness of the scratch was measured.

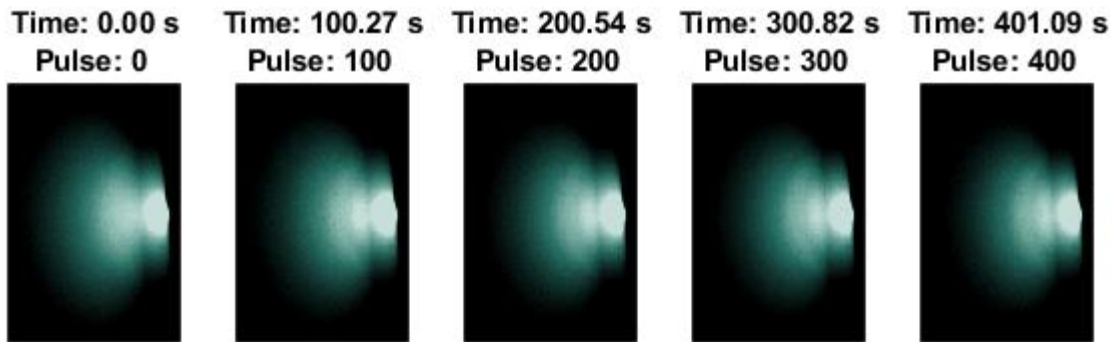


*Figure S3.1.1: RHEED data of an MST film grown at room temperature over an amorphous SiO<sub>x</sub>. The patterns show ring-like features indicative of nanocrystals.*

Once the deposition finished, the film was heated up to 210°C. As can be seen from **Figures S3.1.2**, the ring-like features begin to disappear past 120°C, and by 210°C the pattern once again shows no diffraction, similar to the amorphous SiO<sub>x</sub>. Even if the film is heated to 300°C, the pattern remains unchanged.

Therefore, it is likely that thin layers of MST evaporate before crystallizing, thereby hindering the formation of seeds and thus homoepitaxy.

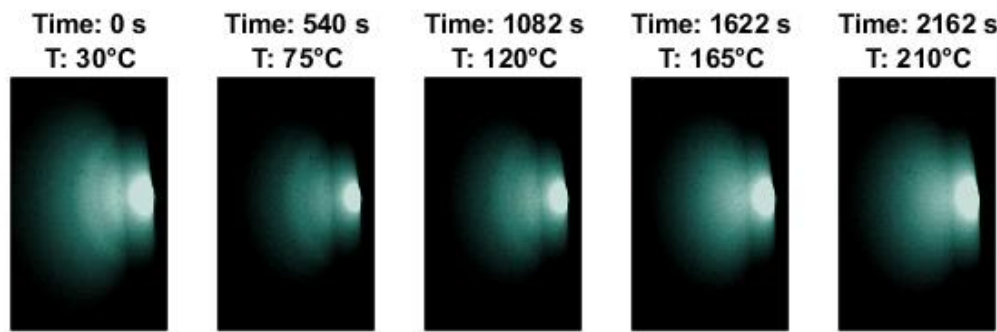


*Figure S3.1.2: Attempt at crystallization of an MST film (400 pulses). No crystallization occurs even when the sample was heated passed 300°C degrees as indicated by the absence of any diffraction.*

### S3.2: Van der Waals epitaxy and thickness limitation.

Next, we show the in-situ RHEED for the heteroepitaxy of MST over  $Sb_2Te_3$  seeds. **Figure S3.2.1** shows the room temperature of  $Sb_2Te_3$  over amorphous  $SiO_x$ . Similar to MST, the pattern also develops rings indicative of nanocrystals, just like **Figure S3.1.1**.

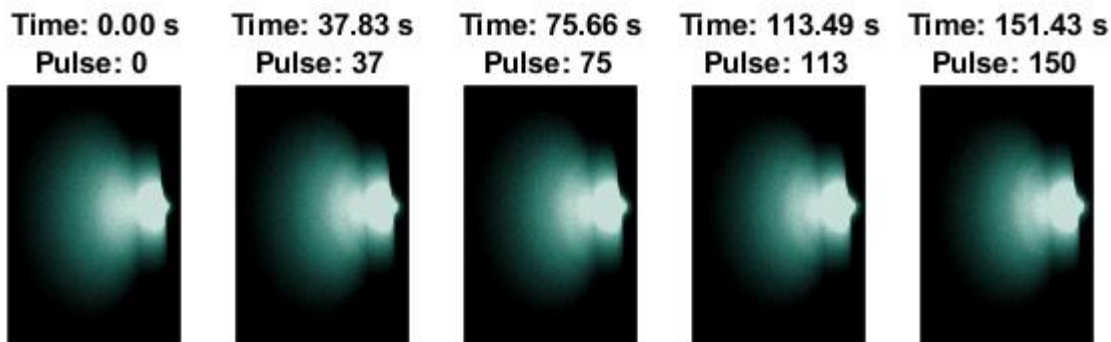


*Figure S3.2.1: RHEED data of an  $Sb_2Te_3$  film grown at room temperature over an amorphous  $SiO_x$ . The patterns show ring-like features indicative of nanocrystals.*

**Figure S3.2.2** shows the crystallization process of those seeds upon annealing. Around 170°C, the RHEED pattern develops streaks indicating that the  $Sb_2Te_3$  has crystallized with an out-of-plane texture. As the temperature increased, the features became more defined. The streak intensity is modulated, suggesting a multi-level surface [Ichimiya, A., & Cohen, P. I. (2004). *Reflection high-energy electron diffraction*. Cambridge University Press].

Before continuing the growth, a waiting period of 10 minutes was employed to stabilized the temperature feedback-loop. **Figure S3.2.3** shows the RHEED pattern for the first 600 pulses. The pattern remains qualitatively similar, but loses intensity over time, as expected from increased roughness and disorder.

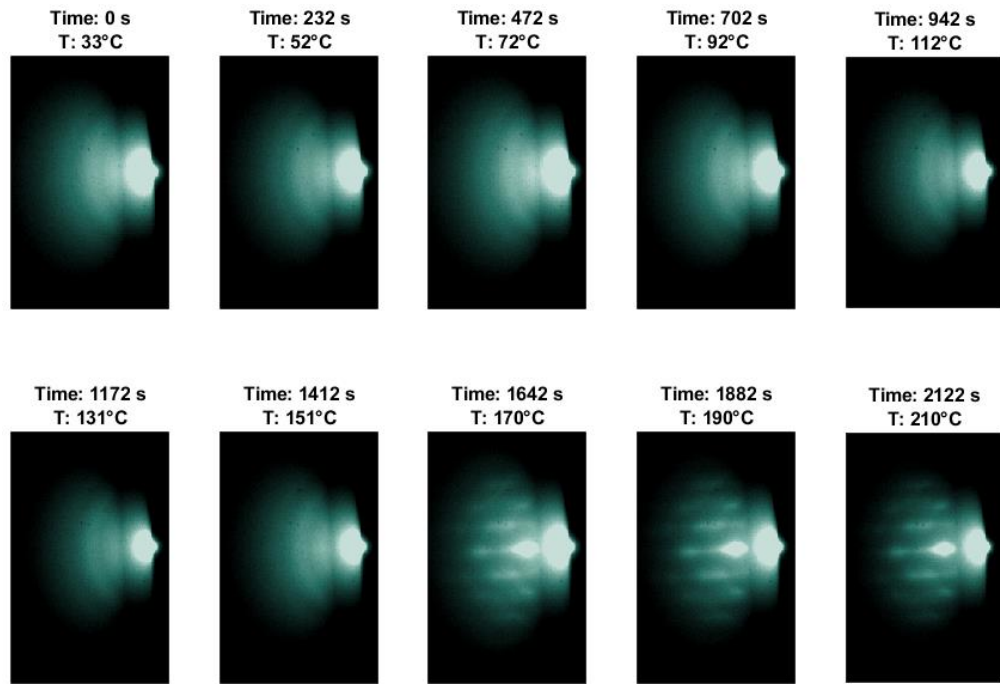


Figure S3.2.2: RHEED pattern showing the crystallization of  $Sb_2Te_3$  seeds after annealing. The appearance of streaks indicates that the film is highly textured.

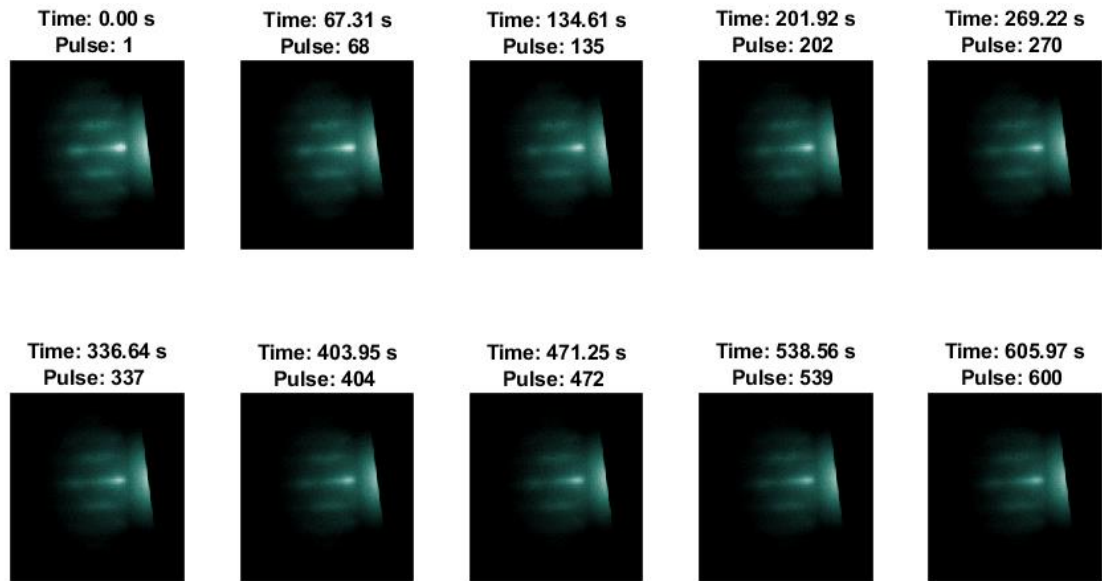


Figure S3.2.3: RHEED pattern during the growth of MST over  $Sb_2Te_3$ . At the beginning of the growth, the RHEED streaks are preserved, indicating epitaxy. The intensity of the pattern diminishes as roughness and disorder increase.

To qualitatively analyze the pattern, the pixel intensities are summed parallel to the direction of the RHEED streak and studied as a function of time. The process is illustrated in **Figure S3.2.4**. The position of the streaks is determined by subtracting a 4<sup>th</sup>-order polynomial background and fitting parabolas to the apex of the peaks, as illustrated in **Figure S3.2.5** for the pure  $Sb_2Te_3$  seeds and the 600<sup>th</sup> pulse of MST.

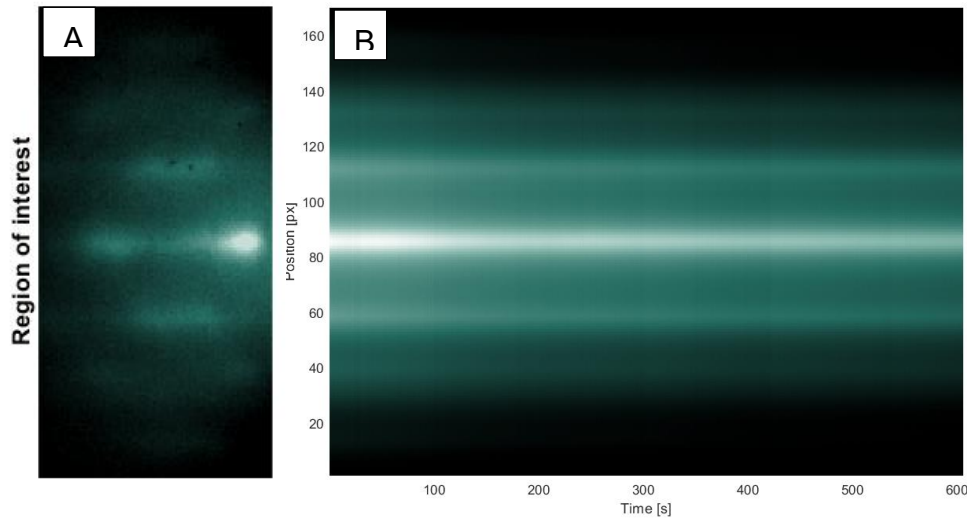


Figure S3.2.4: (A) Region of Interest in the diffraction pattern used to study the development of strain and RHEED oscillations. (B) Integrated intensities along the streaks and their intensity variations over time.

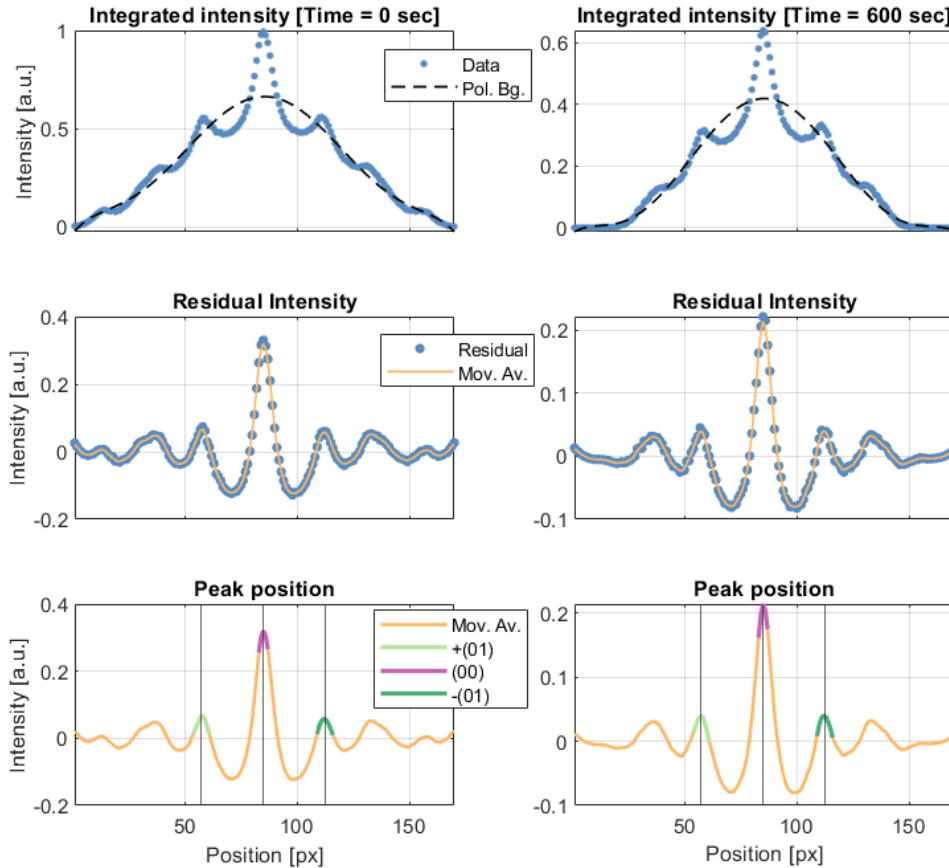


Figure S3.2.5: To study the stress developed during the growth, the position of the streaks is monitored as a function of time. The peaks are found by a quadratic fitting of the maximum after a polynomial background subtraction.

The average separation between the (01) [both left and right] and (00) streaks is plotted in **Figure S3.2.6 (B)**. The distance has a minimal increase (less than  $\frac{1}{2}$  a pixel) as the film grows consistent with the lattice-matched condition of the  $\text{Sb}_2\text{Te}_3$  seeds. The

slight increase points to a shrinkage of the crystal structure consistent with the relaxation of strain built during seeding [Vermeulen. "Growth and nanostructure of tellurides for optoelectronic, thermoelectric and phase-change applications". English. PhD thesis. University of Groningen, 2019. isbn: 978-94-034-1422-5].

The intensity variation of the (00) streak, as determined by averaging the 5 pixels next to the apex, is plotted in **Figure S3.2.6 (A)**. Due to the many grains created during seeding, layer-by-layer growth is not expected; nevertheless, slight intensity oscillations can still be observed, further confirming the results of Van der Waals epitaxy. Note that because the growth is multilevel, the oscillation period does not necessarily indicate the completion of a full layer.

Finally, as the growth progressed, the pattern slowly changed to that presented in **Figure S3.2.7**. The appearance of rings superimposed on the RHEED streaks indicates the presence of particulate/nanocrystals carried by the plume as discussed in section 2.2 of the main text. This stopped epitaxy and thus limited the final film thickness obtained with this procedure.

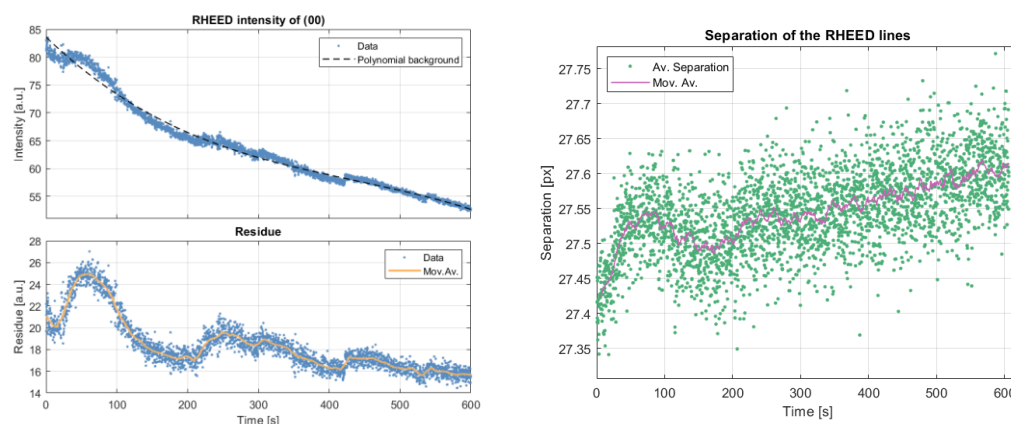


*Figure S3.2.6: (A) Intensity variations of the (00) streak. Courtesy of the many Sb<sub>2</sub>Te<sub>3</sub> seeds, the growth is not layer by layer but multilevel; nevertheless, small oscillations can be observed, corroborating epitaxy. (B) Average separation between the (00) streak and (01) streak and its moving average. The separation increases very slightly (less than ½ a pixel change), consistent with less strain layers at the surface.*



*Figure S3.2.7: Around the 1000<sup>th</sup> pulse, the RHEED pattern slowly changes to a mixture of two diffraction patterns: streaks and rings. This superposition indicates the presence of nanocrystals on top of a textured film.*

#### S4: EDS of solid ingot

To further study the stoichiometry and uniformity of the ingot at a micron-scale, the EDS spectra was measured. **Figure S4.1** shows the identified phases using EDAX TEAM: Texture & Elemental Analytical Microscopy software. The individual signal of the elements composing  $\text{MnSb}_2\text{Te}_4$  is illustrated in **Figure S4.2**; the minimal contrast indicates that those elements are in similar proportions all through the specimen, further corroborating the phase uniformity.

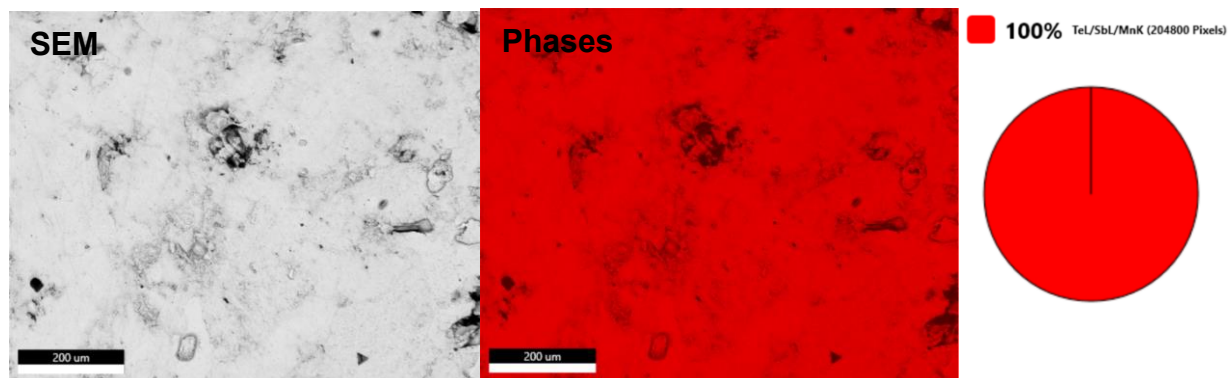


*Figure S4.1: Micrograph of the ingot's polished surface and phase map its corresponding phase map. No additional phases were identified.*

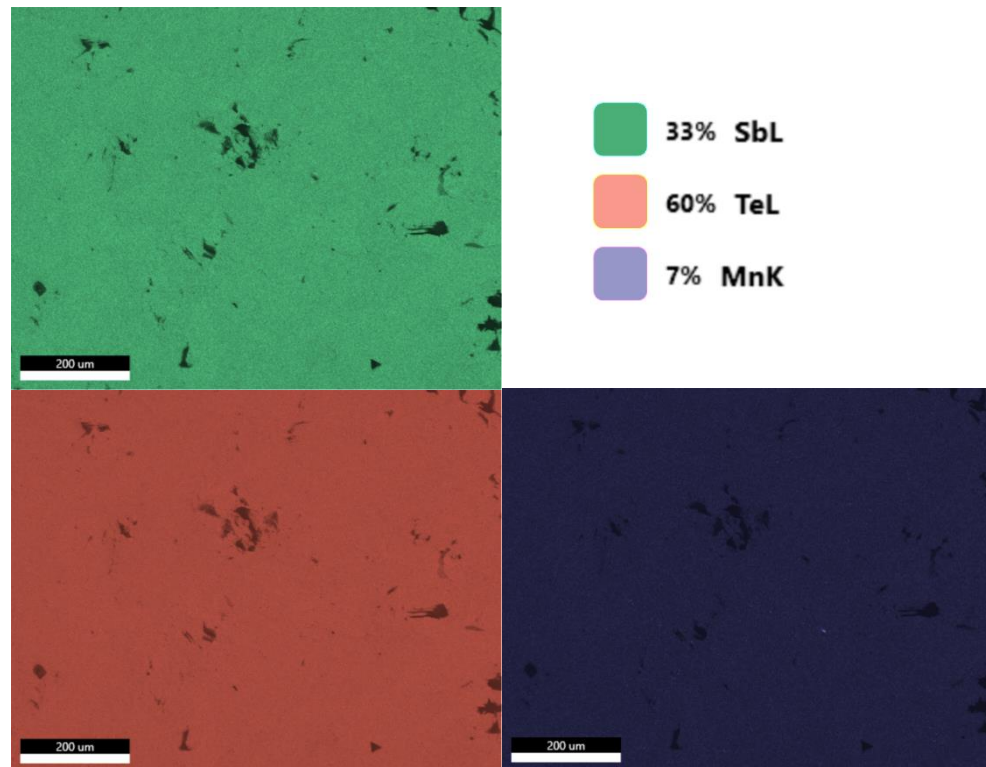


*Figure S4.2: Elemental Overlay of the EDS signal for Sb L-line, Te L-line, and Mn K-line with their respective weight percentage. The uniform intensity of the images indicates that the elements are equally distributed through the material.*

To estimate the composition of the ingot, the EDS spectrum was deconvoluted using the ZAF procedure [Newbury, D. E., & Ritchie, N. W. (2015). Performing elemental microanalysis with high accuracy and high precision by scanning electron microscopy/silicon drift detector energy-dispersive X-ray spectrometry (SEM/SDD-EDS). *Journal of materials science*, 50(2), 493-518.] as implemented in the EDAX TEAM software. The spectrum and its respective deconvolution are graphed in **Figure S4.3**. Additional elemental peaks of background origin were also included in the deconvolution.

The resulting atomic and weight percentages are summarized in **Table S4**; the stoichiometry is in good agreement with the expected composition of  $\text{MnSb}_2\text{Te}_4$  (Atomic: 14.28% Mn, 28.57% Sb, 57.14%).

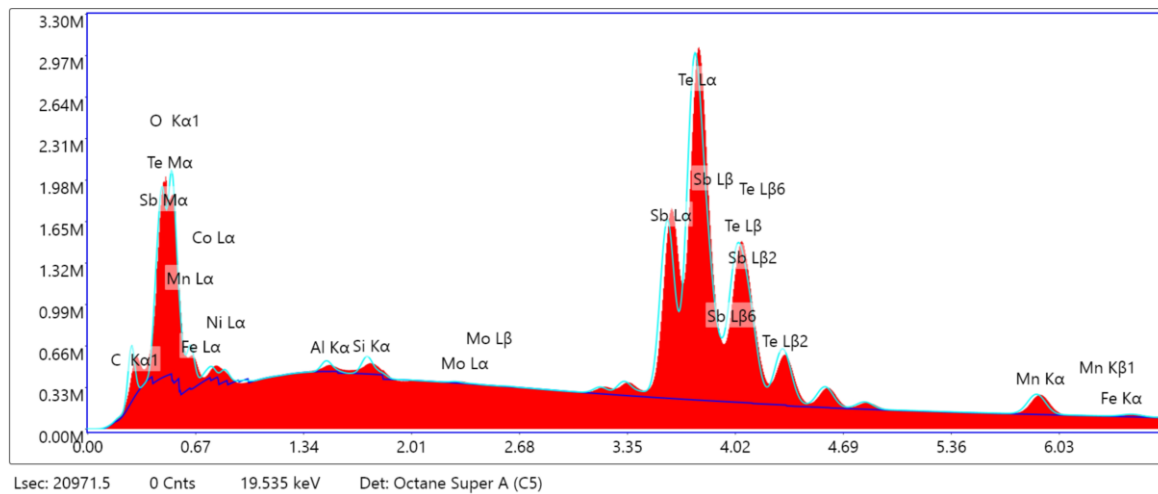


*Figure S4.3: Deconvolution of the total SEM-EDS spectra. Additional background elements (C, O, Fe, Ni, Al, Mo) were included in the deconvolution but excluded from quantification.*

eZAF Smart Quant Results								
Element	Weight%	Atomic%	Net Int.	Error %	Kratio	Z	A	F
SbL	29.60	28.03	1490.50	2.98	0.2868	1.0033	1.0003	1.0046
TeL	63.38	57.26	2728.40	3.07	0.5929	0.9720	1.0010	1.0006
MnK	7.01	14.71	211.90	5.86	0.0831	1.2978	0.9398	1.0109

*Table S4: Results of performing a ZAF analysis on the spectrum in Figure S5.3.*

## S5: Additional atomically-resolved EDS maps

## S5.1: Ingot

In this section, we present additional EDS maps of a single grain of MST. The results are represented in **Figure S5.1**. The measurements were done on a region different from **Figure 3b** of the main text and further corroborate the presence of an asymmetry in the anti-site distribution of Mn in the Sb planes. The structure is observed in all septuple layers. Once again, no site mixing was observed in the Te planes.

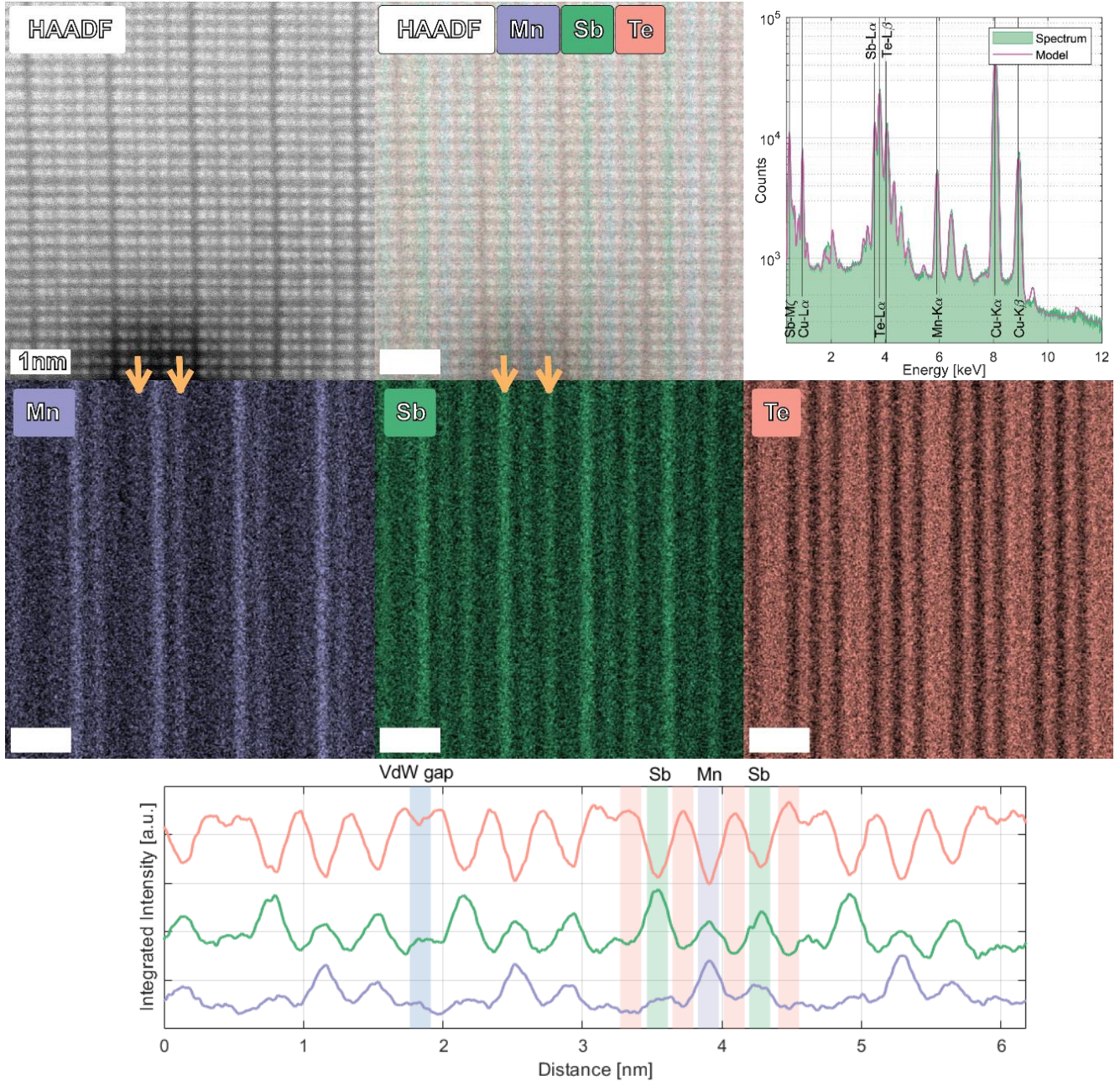


**Figure S5.1:** Additional atomically-resolved EDS-STEM scan (integration over 1092 frames). The measurements were taken over a different region than the one presented in Figure 3a of the main text. Mn-Sb site mixing is confirmed at the atomic scale. The asymmetry between the Sb-planes, marked with orange arrows, is clearly visible.

### S5.2: Additional information on Figure 3

In this section, we present additional analysis on the results presented in **Figure 3** of the main text regarding the single-grain stoichiometry. The total spectrum and its deconvolution are illustrated in **Figure S5.2.1**. The composition was estimated using the Brown–Powell ionization cross-section model as implemented in the Velox Software after a multi-parabolic background correction.

The resulting atomic and weight percentages are summarized in **Table S5.2.1**; the deconvolution is complicated by the fact that Sb-L and Te-L peaks present a significant overlap, thereby considerably increasing the uncertainties in the quantification of those particular elements. Overall, the stoichiometry (atomic: 17.5% Mn, 27.1% Sb, 55.4%) is in good agreement with the results presented in Figure 3d, if slightly Mn-rich.

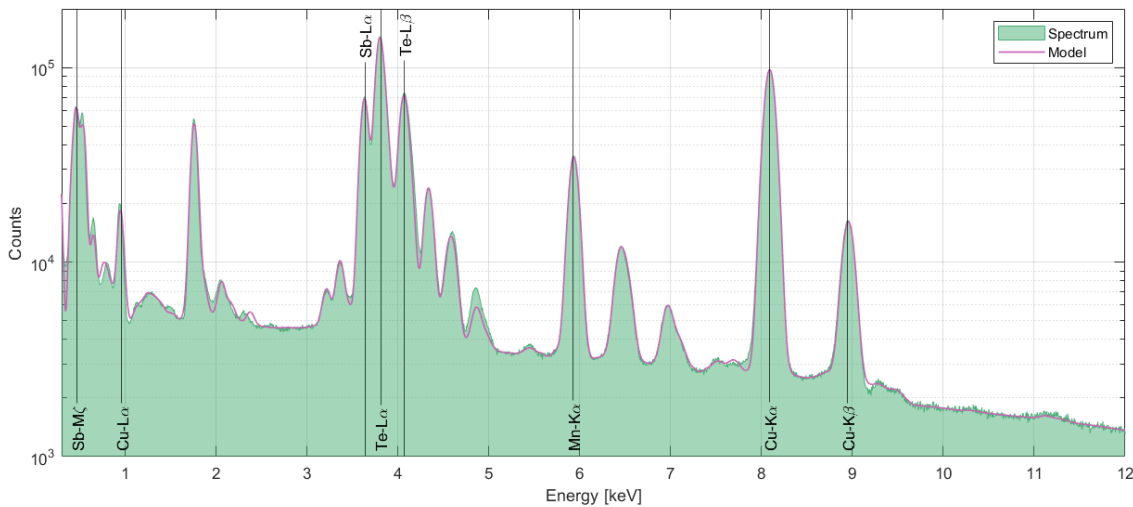


*Figure S5.2.1: Deconvolution of the total spectrum of Figure 3a of the main text. Additional background elements (C, O, Si, Ti, Cr, Fe, Co, Ni, Cu, Ga, Zr, Pt) were included in the deconvolution but excluded from quantification.*

Velox analysis of spectrum (Brown – Powell model)							
Z	Element	Family	Atomic Fraction (%)	Atomic Error (%)	Mass Fraction (%)	Mass Error (%)	Fit error (%)
25	Mn	K	17.50	1.29	8.49	0.70	0.2
51	Sb	L	27.13	2.73	29.16	3.03	0.05
52	Te	L	55.37	3.21	62.35	3.28	0.01

*Table S5.2.1: EDS Quantification of Figure S5.2.1.*

To further quantify the asymmetry between the Sb planes, the spectra recorded from only those planes are studied, as illustrated in **Figure S5.2.2**. The asymmetry between Sb-Mn site mixing is clearly resolved in the Sb-L $\alpha$  and Mn-K $\alpha$  peaks. The quantification of those areas is summarized in **Table S5.2.2**. Note that due to a considerable contribution of the rest of the crystal as a background signal, the percentual differences

between those two areas do not represent a direct measurement of the Mn/Sb perceptual occupancies in those planes.

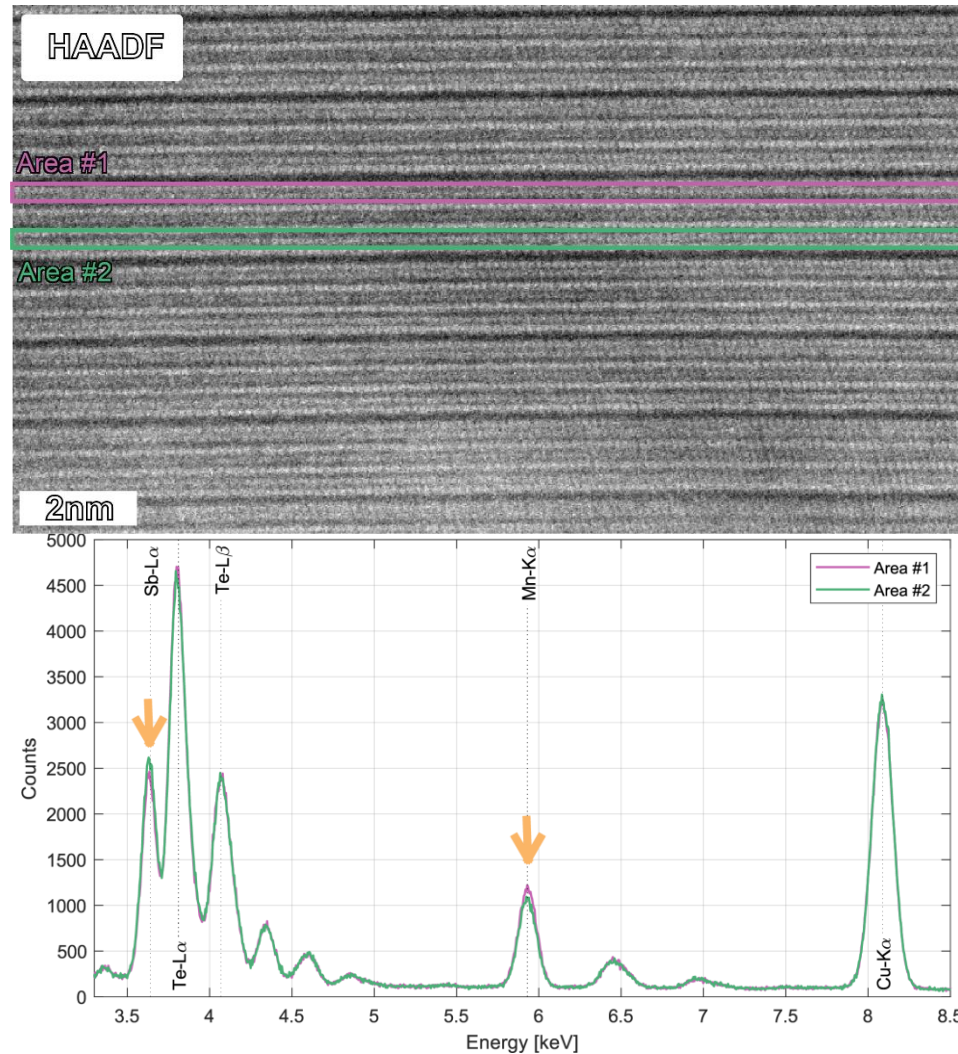


*Figure S5.2.2: Comparison between the two Sb planes. By taking similar areas, the Cu-K $\alpha$  peak is normalized. The asymmetry in Sb and Mn concentration clearly resolved in the Sb-La and Mn-K $\alpha$  peaks.*

Velox analysis of spectrum (Brown – Powell model)							
Z	Element	Family	Atomic Fraction (%)	Atomic Error (%)	Mass Fraction (%)	Mass Error (%)	Fit error (%)
<b>Area #1</b>							
25	Mn	K	17.83	1.29	8.67	0.70	0.07
51	Sb	L	28.32	2.79	30.52	3.10	0.02
52	Te	L	53.85	3.24	60.81	3.34	0.05
<b>Area #2</b>							
25	Mn	K	16.08	1.18	7.74	0.63	0.16
51	Sb	L	30.89	2.96	32.96	3.25	0.08
52	Te	L	53.03	3.31	59.30	3.43	0.05

*Table S5.2.2: EDS Quantification of the areas marked in Figure S5.2.2.*

S5.3: Thin film

In this section, we present the EDS-STEM results of the MST film over  $Sb_2Te_3$  seed; the results are summarized in **Figure 5.3**. Because the film was composed of small grains, elemental atomic resolution could not be obtained; nevertheless, the general distribution of the elements within a septuple layer could still be resolved. For instance, Mn appears to occupy only the middle layer of the septuple, while Sb populates both the Sb and Mn planes. The broadness of the Sb peaks also suggests some level of intermixing within the Te planes, but cannot be definitely concluded due to the poor signal-to-noise ratio.

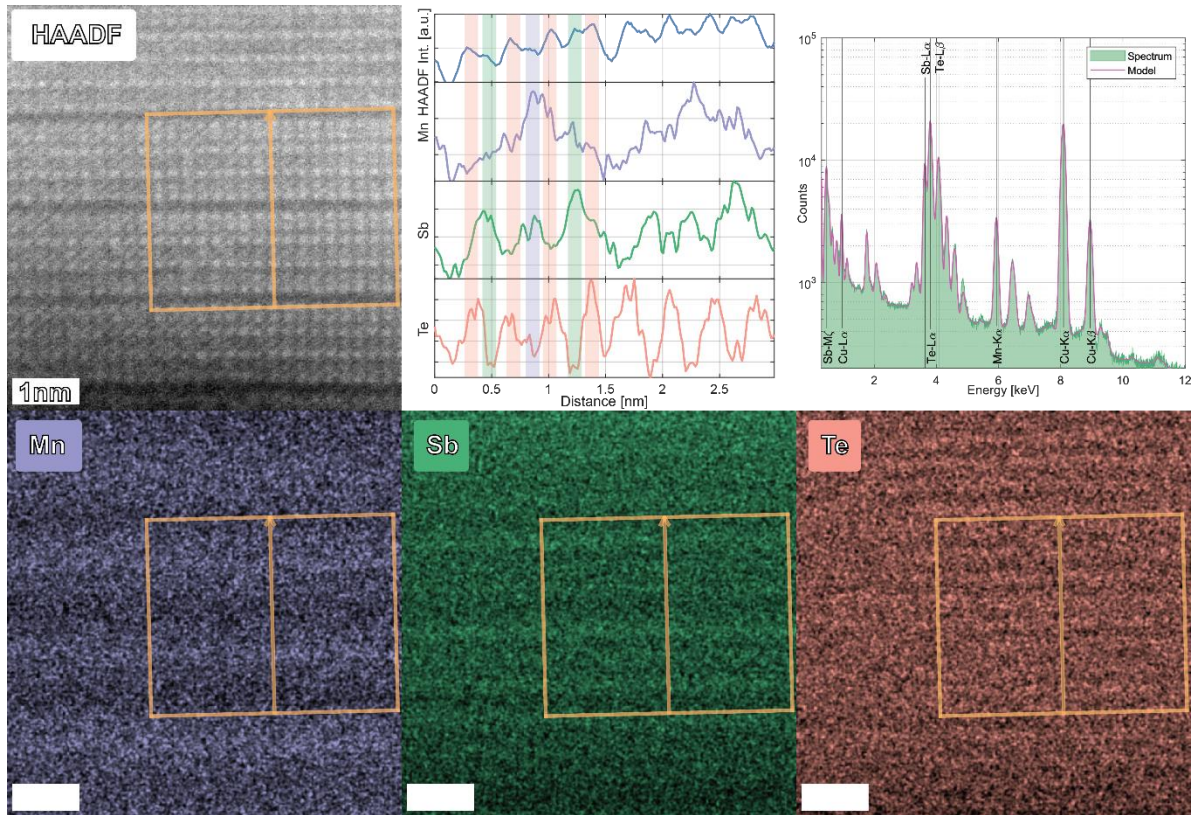


*Figure S5.3: EDS-STEM elemental map of the MST film over  $Sb_2Te_3$  seeds. The Mn signal is mostly concentrated in the middle of the septuple, while Sb could be found both in the Sb and Mn planes.*

## S6: Additional magnetization plots

In this section, we present the results of additional field cooling experiments at different fields. For weak field strengths, the magnetization develops a maximum as indicated in the main text (section 4). **Figure S6** shows that when the magnitude of the field increases, the maximum shifts to lower temperatures until it fully disappears at a moderate field strength. Indeed, at a value of 0.5T, the feature is fully absent and the curve is reminiscent of a ferromagnet.

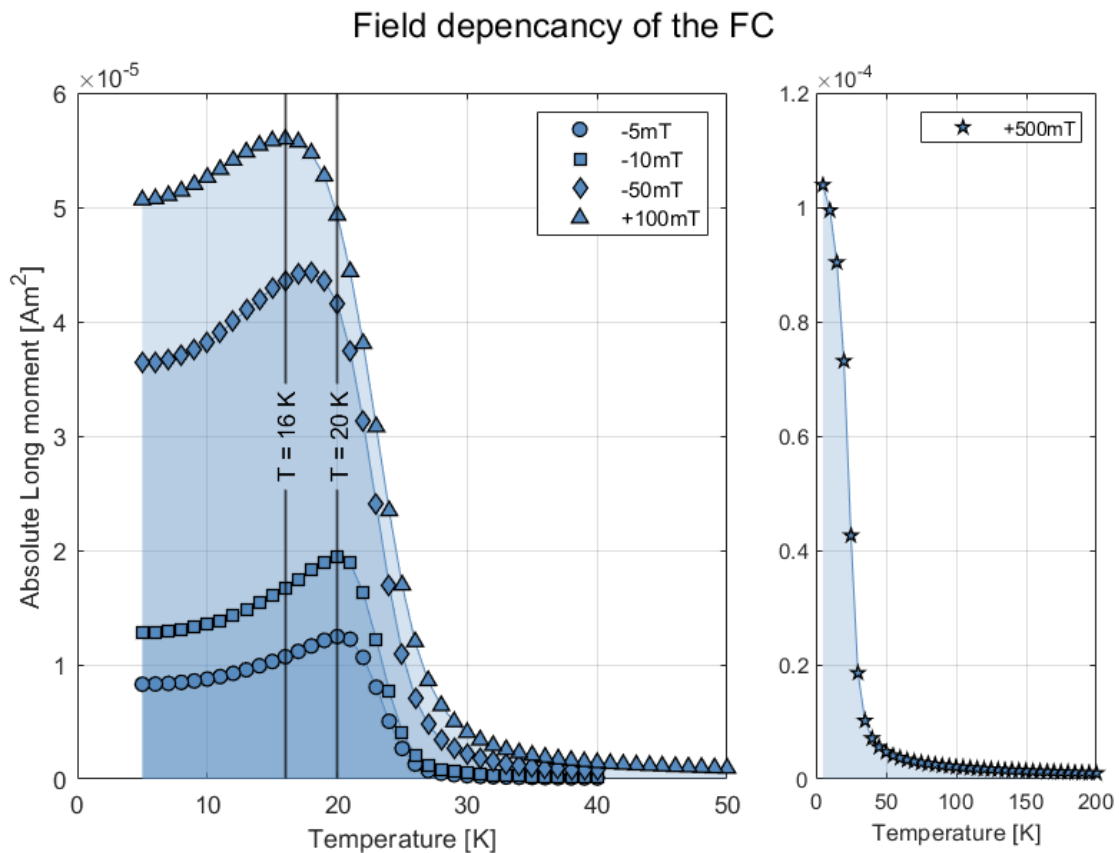


*Figure S6: Field dependency of the magnetization upon field cooling. The maximum shifts to lower values of temperature and eventually disappears at moderate field strength.*